The Astrophysical Journal, 860:55 (25pp), 2018 June 10 https://doi.org/10.3847/1538-4357/aac2d8

An Analytic Formulation of the 21 cm Signal from the Early Phase of the Epoch of Reionization

Janakee Raste[1,2] and Shiv Sethi[1]
[1] Raman Research Institute, Bangalore 560080, India
[2] Joint Astronomy Program, Indian Institute of Science, Bangalore 560012, India
Received 2017 August 21; revised 2018 May 4; accepted 2018 May 4; published 2018 June 12

Abstract

We present an analytic formulation to model the fluctuating component of the H I signal from the epoch of reionization during the phase of partial heating. During this phase, we assume self-ionized regions, whose size distribution can be computed using excursion set formalism, to be surrounded by heated regions. We model the evolution of the heating profile around these regions (near zone) and their merger into the time-dependent background (far zone). We develop a formalism to compute the two-point correlation function for this topology, taking into account the heating autocorrelation and heating-ionization cross-correlation. We model the ionization and X-ray heating using four parameters: efficiency of ionization, ζ; number of X-ray photons per stellar baryon, $N_{\rm heat}$; spectral index of X-ray photons, α; and minimum frequency of X-ray photons, $\nu_{\rm min}$. We compute the H I signal in the redshift range $10 < z < 20$ for the ΛCDM model for a set of these parameters. We show that the H I signal for a range of scales 1–8 Mpc shows a peak strength of 100–1000 $({\rm mK})^2$ during the partially heated era. The redshift at which the signal makes a transition to a uniformly heated universe depends on the modeling parameters; e.g., if $\nu_{\rm min}$ is changed from 100 eV to 1 keV, this transition moves from $z \simeq 15$ to $z \simeq 12$. This result, along with the dependence of the H I signal on the modeling parameters, is in reasonable agreement with existing results from N-body simulations.

Key words: cosmology: theory – dark ages, reionization, first stars

1. Introduction

The probe of the epoch of reionization (EoR) remains one of the outstanding aims of modern cosmology. In the past 15 yr, important strides have been made in this direction, mainly led by the detection of the Gunn–Peterson effect at $z \simeq 6$ and the cosmic microwave background (CMB) temperature and polarization anisotropy detections by *WMAP* and *Planck* (Fan et al. 2000; Becker et al. 2001; Hinshaw et al. 2013; Planck Collaboration et al. 2014, 2016). The former discovery suggests that the universe could be making a transition from neutral to fully ionized at $z \simeq 6$, while the latter shows that the universe might have been fully ionized at $z \simeq 8.5$. The current best bounds on the reionization optical depth from *Planck* put stringent constraints on the redshift of reionization: $z_{\rm reion} = 8.5 \pm 1$ (Planck Collaboration et al. 2016).

One important missing piece in these probes is that neither seems capable of discerning the dynamics of the reionization process. For instance, the CMB anisotropies (both polarization and temperature) are sensitive only to the integrated optical depth through the surface of reionization (e.g., Dodelson 2003).

Theoretical estimates suggest that the dark age of the universe might have ended around $z \simeq 30$ with the formation of the first structures in the universe. These structures are expected to emit UV light, which might have reionized the universe at $z \simeq 9$ (see, e.g., Barkana & Loeb 2001; Morales & Wyithe 2010; Pritchard & Loeb 2012; Natarajan & Yoshida 2014 and references therein). The most direct way to probe this transition is through the detection of the redshifted hyperfine 21 cm line of neutral hydrogen (H I). The past decade has seen major progress on both the theoretical and experimental front in this endeavor. Currently, there are many ongoing experiments that are attempting to detect both the global H I signal and its fluctuating component from the epoch of reionization. The H I signal from the epoch has been computed both analytically and using numerical simulations. Theoretical estimates show that the global signal is observable in both absorption and emission, with its strength in the range −200–20 mK in a frequency range of 50–150 MHz, which corresponds roughly to a redshift range $25 > z > 8$ (e.g., Madau et al. 1997; Tozzi et al. 2000; Gnedin & Shaver 2004; Sethi 2005). The fluctuating component of the signal is likely to be an order of magnitude smaller on scales in the range 3–100 Mpc, which implies angular scales in the range $\simeq 1'$–$30'$ (e.g., Furlanetto et al. 2004a, 2004b; Zaldarriaga et al. 2004; Pritchard & Furlanetto 2007; for comprehensive reviews, see, e.g., Morales & Wyithe 2010; Pritchard & Loeb 2012; Natarajan & Yoshida 2014). Many of the ongoing and upcoming experiments have the capability to detect this signal in hundreds of hours of integration (e.g., Mesinger et al. 2014; Ahn et al. 2015a). Upper limits on the fluctuating component of the H I signal have been obtained by many ongoing experiments: GMRT, MWA, PAPER, and LOFAR (Paciga et al. 2013; Ali et al. 2015; Beardsley et al. 2016; Patil et al. 2017). The best current upper limits correspond to $k^3P(k)/(2\pi^3) < (22.4\,{\rm mK})^2$ for $0.15 < k < 0.5\,{\rm h\,Mpc^{-1}}$ at $z \simeq 8.4$ (Ali et al. 2015).

The H I signal carries crucial information about the first sources in the universe. In particular, the H I signal is determined by the radiation emitted by these sources in three frequency bands: UV radiation that ionizes the medium, Lyα radiation (frequencies between the Lyman limit and Lyα), and X-ray photons (all photons with energies much higher than the hydrogen and helium ionization threshold). The emission in these three bands determines the evolution of the global H I signal. And, along with primordial density perturbations given by the ΛCDM model, the perturbations of these radiation fields

establish the length scales of the fluctuating component of the signal.

In this paper, our main focus is the analytic modeling of the fluctuating component of the H I signal in its early phase when the universe is partially heated. This phase of the EoR has been extensively studied using numerical methods and analytic estimates (e.g., Pritchard & Furlanetto 2007; Mesinger et al. 2011; Visbal et al. 2012; Mesinger et al. 2013; Tashiro & Sugiyama 2013; Pacucci et al. 2014; Fialkov et al. 2014; Ghara et al. 2015; Fialkov et al. 2017). We present a new formalism in this paper that seeks to unravel the correlation structure of the fluctuations based on the topology of the ionization and heating regions.

In the next section, we review the H I signal from the epoch of reionization and discuss the impact of three radiation fields on the signal. In particular, the modeling of X-ray heating is described in detail. In Section 3, we present our formalism for computing the two-point correlation function of the H I signal. We also discuss various approximations, assumptions, and limits germane to our formulation. In Section 4, we present our results and compare them with the inferences of other studies. In Section 5, we summarize our findings and make concluding remarks. Throughout this paper, we assume the spatially flat ΛCDM model with the following parameters: $\Omega_m = 0.254$, $\Omega_B = 0.049$, $h = 0.67$, and $n_s = 0.96$, with the overall normalization corresponding to $\sigma_8 = 0.83$ (Planck Collaboration et al. 2016).

2. Cosmic Dawn and Epoch of Reionization

In the rest frame, hyperfine splitting of the ground state of neutral hydrogen causes an energy difference that corresponds to a wavelength $\lambda = 21.1$ cm. The excitation temperature of this line, T_S, is determined by three processes in the early universe: emission and absorption of CMB photons, which is a blackbody of temperature $T_{\rm CMB}$; collisions with atoms; and the mixing of the two levels caused by Lyα photons (the Wouthuysen–Field effect). Here T_S can be expressed in terms of the color temperature of Lyα photons, T_α; gas kinetic temperature, T_K; and $T_{\rm CMB}$ (Field 1958; Pritchard & Loeb 2012):

$$T_S = \frac{T_{\rm CMB} + y_\alpha T_\alpha + y_c T_K}{1 + y_\alpha + y_c}. \tag{1}$$

Here $y_c \propto n_{\rm H}$ and $y_\alpha \propto n_\alpha$ ($n_{\rm H}$ and n_α are the number densities of neutral hydrogen atoms and Lyα photons, respectively) determine the efficiency of collisions and Lyα photons, respectively. In the early universe, $1000 < z < 100$, T_S relaxes to $T_{\rm CMB}$. In the redshift range $100 < z < 30$, collisions determine the spin temperature, and T_S relaxes to the kinetic temperature T_K of the matter. As the epoch of reionization commences, the production of Lyα photons couples the spin temperature to the color temperature of Lyα T_α. It can be shown that multiple scattering of Lyα photons with H I causes T_α to relax to the kinetic temperature (e.g., Field 1959; Rybicki & dell'Antonio 1994; Chen & Miralda-Escudé 2004). Therefore, if $y_{\rm tot} = y_c + y_\alpha \gtrsim T_{\rm CMB}/T_K$, then T_S is strongly coupled to T_K. Otherwise, it relaxes to $T_{\rm CMB}$.

The H I emits or absorbs 21 cm radiation from the CMB depending on whether its T_S is greater than or less than $T_{\rm CMB}$. This temperature difference is observable and can be expressed as (e.g., Madau et al. 1997; Shaver et al. 1999; Gnedin & Shaver 2004; Sethi 2005; Pritchard & Loeb 2012)

$$\begin{aligned}\Delta T_b &= \frac{1 - e^{-\tau}}{1 + z}(T_S - T_{\rm CMB}) \simeq \frac{\tau}{1 + z}(T_S - T_{\rm CMB}) \\ &\simeq 26.25\, n(1 + \delta)\left(1 - \frac{T_{\rm CMB}}{T_S}\right) \\ &\quad \times \left(\frac{1 + z}{10}\frac{0.14}{\Omega_m h^2}\right)^{\frac{1}{2}}\left(\frac{\Omega_b h^2}{0.022}\right) {\rm mK}.\end{aligned} \tag{2}$$

Here we ignore redshift space distortion. In writing the expression, we have expressed the H I number density as $n_{\rm H} = \bar{n}_{\rm H} n(1 + \delta)$; δ corresponds to density inhomogeneities in the gas. The value of the mean density $\bar{n}_{\rm H}$ has been absorbed in the prefactor of Equation (2). In our formulation, every small volume is either completely neutral or completely ionized; therefore, we define a variable n, which is unity if the medium is neutral and zero otherwise. In addition to density inhomogeneities, there are ionization and spin temperature, T_S, inhomogeneities (as the medium is partially ionized or partially heated). We further define dimensionless temperature fluctuation as (Zaldarriaga et al. 2004)

$$\psi = n(1 + \delta)\left(1 - \frac{T_{\rm CMB}}{T_S}\right) = n(1 + \delta)(1 - s). \tag{3}$$

We have defined $s = T_{\rm CMB}/T_S$. The statistics of ψ allows us to study the main physical processes that cause brightness temperature fluctuations: δ (density perturbations), n (ionization inhomogeneities), and s (fluctuations of spin temperature). All these quantities are functions of position in space, but we suppress this dependence for notational clarity. In this paper, we assume $T_\alpha = T_K$ everywhere, as discussed in Section 2.3.

We next consider the impact of the three radiation fields—ionizing radiation, Lyα photons, and X-ray photons—on the brightness temperature inhomogeneities.

2.1. Photoionization

At the end of the dark ages, high-density regions of the universe collapse and form structures of different masses. In our work, we assume that the smallest mass that can collapse corresponds to the H I–cooled halo (e.g., Barkana & Loeb 2001):

$$M_{\rm min} = 3.915 \times 10^8 \frac{\Omega_m^{1/2}}{h\,(1 + z)^{3/2}}\, M_\odot. \tag{4}$$

These collapsed structures emit UV photons, which are absorbed in the immediate vicinity of the sources and carve out H II regions around them in the intergalactic medium (IGM). These structures also emit Lyα and X-ray radiation, which penetrates further into the IGM.

The size distribution of the ionization bubbles can be computed using excursion set formalism by defining self-ionized regions (Furlanetto et al. 2004a). These regions have enough sources to ionize all the gas in them. Such regions are not created by a single source but rather a set of highly clustered sources, which is the case in the early universe for the ΛCDM model; therefore, these regions are larger than the H II regions of a single source. Here we briefly describe the

formalism (for details, see, e.g., Furlanetto et al. 2004a and references therein). We start by defining ζ, the ionization efficiency factor:

$$\zeta = f_\star f_{\rm esc} N_{\rm ion} N_{\rm rec}^{-1}. \quad (5)$$

Here $f_\star$ is the fraction of collapsed baryons that is converted into stars, $f_{\rm esc}$ equals the fraction of ionizing photons that escape the source halo, $N_{\rm ion}$ is the number of hydrogen-ionizing (UV) photons created per stellar baryon, and $N_{\rm rec}$ is the number of recombinations. We assume ζ to be constant in this paper, even though it could be time-dependent owing to the evolution of the quantities used to define it. Inside a self-ionization region, $1/\zeta = f_{\rm coll} = M_{\rm coll}/M_{\rm tot}$, where $f_{\rm coll}$ is the fraction of collapsed mass inside the self-ionized region.

Using the extended Press–Schechter model, the collapse fraction can be expressed as

$$f_{\rm coll} = {\rm erfc}\left[\frac{\delta_c(z) - \delta_m}{\sqrt{2[\sigma^2_{\rm min} - \sigma^2(m)]}}\right].$$

Here $\sigma^2(m)$ is the variance of the density fluctuations for mass m, the mass of the self-ionized region at $z = 0$; $\sigma^2_{\rm min} \equiv \sigma^2(m_{\rm min})$; and $\delta_c(z) = 1.68/D_+$, the critical density for collapse at redshift z and D_+ is the growing mode of the density perturbations. Here $\delta_x(m, z)$ is the redshift and mass-dependent barrier for excursion set formalism. The linear fit to this true barrier at $m \to \infty$ is

$$B(m, z) = \delta_c(z) - \sqrt{2}\, K(\zeta)\sigma_{\rm min} + \frac{K(\zeta)\sigma^2(m)}{\sqrt{2}\,\sigma_{\rm min}},$$

where $K(\zeta) = {\rm erf}^{-1}(1 - \zeta^{-1})$. To find the self-ionized region, we need to find the first up-crossing of δ above the curve described by $B(m, z)$. We can write the mass function analytically as (Sheth 1998)

$$m\frac{dn}{dm} = \sqrt{\frac{2}{\pi}}\frac{\bar{\rho}}{m}\left|\frac{d\ \ln\sigma}{d\ \ln m}\right|\frac{B_0}{\sigma(m)}\exp\left[-\frac{B^2(m, z)}{2\sigma^2(m)}\right], \quad (6)$$

where $B_0 \equiv \delta_c(z) - \sqrt{2}\, K(\zeta)\sigma_{\rm min}$ is the value of the barrier at $m \to \infty$. Equation (6) gives the comoving number density of the self-ionized bubbles in the mass range $(m, m + dm)$. Here $\bar{\rho}$ is the background mass density. We use the ΛCDM power spectrum (the matter power spectrum of the ΛCDM model is generated using the publicly available code CMBFAST) for solving Equation (6). We note that this formalism has been used extensively for analytic work and for simulations of the epoch of reionization, including in the publicly available code 21 cmFAST (Mesinger et al. 2011). In a numerical simulation, the self-ionized region is constructed by identifying the largest contiguous region that satisfies the condition for a self-ionized bubble: $f_{\rm coll} = 1/\zeta$. This region need not be spherical. For analytic work, we assume the region to be spherical. We discuss the implications of this assumption in a later section.

Figure 1 shows the effect of ζ on the global ionization fraction f_i of the universe. For a higher value of ζ, the reionization is completed at a higher redshift. In Figure 2, we show the distribution of the volume fraction occupied by bubbles of different sizes and its evolution with redshift. We show the volume fraction as a function of halo mass, which can be related to the comoving size of the self-ionized bubble as $R_x \simeq 0.09\ {\rm Mpc}(M/10^8\ M_\odot)^{1/3}\zeta^{1/3}$. Figure 2 agrees with the results of Furlanetto et al. (2004a; their Figure 2) for the set of parameters used by them. For the set of parameters used in this paper, the self-ionized bubbles are smaller; e.g., at $z = 12$, the peak of the bubble distribution corresponds roughly to a scale of $R_x \simeq 10$ Mpc for Furlanetto et al. (2004a), while it peaks at $R_x \simeq 3$ Mpc for our case.

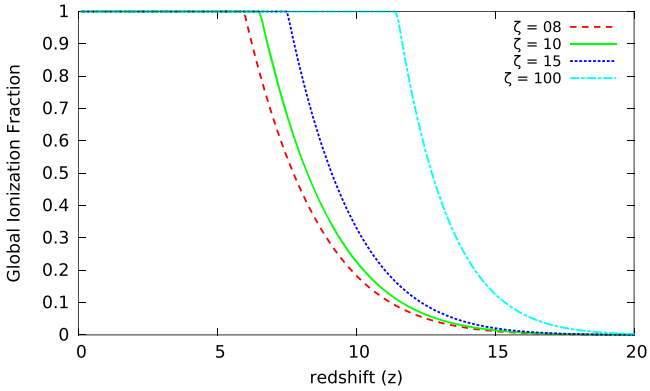

Figure 1. Evolution of the global ionization fraction (f_i) for different values of ζ.

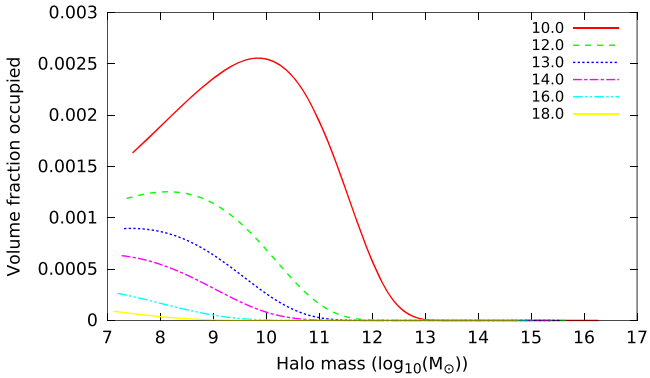

Figure 2. Evolution of the size distribution of self-ionized regions as a function of halo mass for $\zeta = 10$.

2.2. X-Ray Heating

Photons of energy $E \gg 13.6$ eV are not absorbed in the H II region but escape into the surrounding medium. These photons ionize and heat the medium through photoionization and secondary collisional ionization and excitation. These photons can ionize the medium to a level of less than 10% and impart up to 20% of their total energy into heating the medium (e.g., Shull & van Steenberg 1985; Venkatesan et al. 2001). As the fraction of ionization in this process is generally tiny, in our study, we assume the medium outside the ionized region to be comprised of neutral hydrogen and neutral helium with primordial abundances. We hope to study the effect of partially ionized regions in future work.

A key fact in X-ray heating of the mostly neutral gas outside the H II region is that the photoionization cross section falls as $1/\nu^3$ for energies far larger than the threshold energy. As the low-energy X-ray photons are absorbed with higher probability, they contribute to heating the medium immediately surrounding the H II region, whereas the higher-energy photons free-stream through the medium. As they are redshifted, their

probability of absorption slightly increases. These photons uniformly heat up the whole IGM to some background temperature $T_{\rm bg}$.

In this section, we calculate the profile of the kinetic temperature around the self-ionized regions. In our analysis, we separate the regions into near and far zones. In the near zone, the heating is dominated by X-ray photons from an individual self-ionized region. In the far zone, the contribution from only the faraway background sources is taken into account.

2.2.1. Near Zone

To compute the temperature profile for an individual source at a redshift z, we calculate the total energy absorbed (over the entire history of the source) by a point close to the source at redshift z'. In this subsection and the following one, primed quantities are calculated at the receiving point (point P), unprimed quantities are at the source (point S), and quantities with a 0 subscript are comoving quantities.

The energy attained by electrons due to the ionization of species i (here i runs over hydrogen and neutral helium with their relative fractions $x_i = 12/13$ and $1/13$ of the baryon number, respectively) per unit time per unit comoving volume per unit frequency (at P) is

$$\frac{dE'_{\nu'}(i)}{dt' d\nu' dV_0} = (h\nu' - h\nu_i)\frac{dN'_{\nu'}}{dt' d\nu' dV_0} P(i, \nu'). \tag{7}$$

Here $dN'_{\nu'}/(dt' d\nu' dV_0)$ is the number of X-ray photons (of frequency ν') received per unit time per unit frequency per unit comoving volume, and $P(i, \nu')$ gives the probability of the ionization of species i by a photon of frequency ν' in a shell of thickness dl':

$$P(i, \nu') = n'_i \sigma_i(\nu') dl'. \tag{8}$$

Here $n'_i = x_i n_0 (1+z')^3$ is the local number density of species i, and σ_i (ν') is the ionization cross section of an atom by an X-ray photon of frequency ν'[3],

$$\sigma_i(\nu') = \sigma_{i0}\left(\frac{\nu'}{\nu_i}\right)^{-3}, \tag{9}$$

with ν_i being the ionization threshold of species i. We assume the X-ray photon luminosity to be given by a power law (e.g., Mesinger et al. 2011 and references therein),

$$\dot{N}_\nu = \dot{N}_t \left(\frac{\nu}{\nu_{\rm min}}\right)^{-\alpha}, \tag{10}$$

where $\nu_{\rm min}$ is the lowest frequency (in the rest frame of the source) of X-ray photons escaping from ionizing sources. We also have

$$\frac{d\dot{N}'_{\nu'}}{d\nu'} = \frac{d\dot{N}_\nu}{d\nu} e^{-\tau(R_0,\nu')}. \tag{11}$$

The optical depth between two points separated by a comoving distance R_0 is given by $\tau(R_0, \nu') = \int \sum_i P(i, \nu')$.

We calculate the X-ray luminosity of a self-ionized region following the prescription of the last section, which allows us to relate $\dot{N}_t$ to ζ (Equation (5)) and the comoving radius of the self-ionized region R_x,

$$\begin{aligned}\dot{N}_t &= \frac{\text{Number of X-ray photons emitted}}{\text{time}} \\ &= \frac{\text{Number of X-rays emitted}}{\text{Number of Baryons in stars}} \\ &\quad \times \frac{\text{Number of Baryons in stars}}{\text{Number of Collapsed Baryons}} \\ &\quad \times \frac{\text{Number of Collapsed Baryons}}{\text{Time}} \\ &= N_{\rm heat} f_\star \frac{d(N_{\rm halo} f_{\rm coll,ion})}{dt},\end{aligned} \tag{12}$$

where $N_{\rm heat}$ is the number of X-ray photons emitted per stellar baryons, $f_\star$ is the fraction of collapsed baryons that is converted into stars, $N_{\rm halo} = 4\pi/3 R_x^3 n_0$ is the number of baryons in a self-ionized region of radius R_x, and $f_{\rm coll,ion} = 1/\zeta$ is the collapsed fraction in an ionized region. We further assume that the collapsed fraction inside an ionization region follows the global collapsed fraction, $f_{\rm coll,g}$, which we obtain from the excursion set formalism. This gives us

$$\frac{d(N_{\rm halo} f_{\rm coll,ion})}{dt} = \frac{1}{\zeta} N_{\rm halo} \frac{\dot{f}_{\rm coll,g}}{f_{\rm coll,g}}. \tag{13}$$

Using Equations (7)–(13), using $dV_0 = 4\pi R_0^2 dR_0$, adding a contribution due to all the species, and integrating over all the frequencies $\nu > \nu_{\rm min}$, we get the energy that goes into heating the medium per unit time per unit volume,

$$\begin{aligned}\frac{dE'_{\rm heat}}{dt' dV_0} = &\frac{h f_{\rm H} \alpha N_{\rm heat} f_\star n_0^2 \nu_{\rm min}^\alpha}{3\zeta} \frac{R_x^3}{R_0^2} \frac{(1+z')^{\alpha+3}}{(1+z)^{\alpha+1}} \frac{\dot{f}_{\rm coll,g}}{f_{\rm coll,g}} \\ &\times \int_{\nu'_{\rm min}}^\infty \nu'^{-\alpha-4} e^{-\tau(R_0,\nu')} \sum_i (\nu' - \nu_i) x_i \sigma_{i0} \nu_i^3 d\nu',\end{aligned} \tag{14}$$

where $\nu'_{\rm min} = \nu_{\rm min}(1+z')/(1+z)$ = the minimum frequency from the source that reaches P. We assume that $f_{\rm H} = 0.15$ is the fraction of the energy of the emitted photoelectrons that goes into heating the medium (Shull & van Steenberg 1985; Venkatesan et al. 2001).

Equation (14) gives the energy that goes into heating the medium by X-ray photons per unit time per unit comoving volume at a distance R_0 from the center of a self-ionized bubble of radius R_x. To get the total increase in temperature due to this heating, we need to integrate this over time. If z'_c is the redshift at which we compute the heating profile, then to take into account the adiabatic cooling since higher redshift z', we multiply by $(1+z'_c)^2/(1+z')^2$. We neglect all other cooling processes. Here $R_x(t')$, the radius of the given ionization region at time t' in the past, is not a straightforward quantity to calculate, as excursion set formalism does not give the time evolution of the radius of a particular self-ionized region. Given that the formalism allows us to compute the evolution of the average ionized fraction f_i, we assume

[3] We use here the approximate expressions for the frequency dependence of the ionization cross section of hydrogen and neutral helium; for more precise formulae, see, e.g., Osterbrock (1989). Our results are not affected by this choice.

$R_x^3(t') = R_x^3(t)(f_i(t')/f_i(t))$. This gives

$$\frac{dE'_{\rm heat}}{dV_0} = \frac{hf_{\rm H}\alpha N_{\rm heat} f_\star n_0^2 \nu_{\rm min}^\alpha}{3\zeta}\frac{R_x^3}{R_0^2}(1+z_c')^2 \times \int_{t(z_\star)}^{t(z_c)} dt' \frac{f_i(t')}{f_i(t)}\frac{\dot{f}_{\rm coll,g}}{f_{\rm coll,g}}\left(\frac{1+z'}{1+z}\right)^{\alpha+1} \times \int_{\nu'_{\rm min}}^{\infty} d\nu' \nu'^{-\alpha-4} e^{-\tau(R_0,\nu')}\sum_i (\nu'-\nu_i)x_i\sigma_{i0}\nu_i^3. \quad (15)$$

Finally, this allows us to compute the increase in temperature due to a self-ionized region of radius R_x at a distance R_0 from the center of the ionized region:

$$\Delta T' = \frac{1}{n_0 k_B}\frac{dE'_{\rm heat}}{dV_0} = \frac{hf_{\rm H}\alpha N_{\rm heat} f_\star n_0 \nu_{\rm min}^\alpha}{3k_B\zeta}\frac{R_x^3}{R_0^2}(1+z_c')^2 \times \int_{t(z_\star)}^{t(z_0)} dt' \frac{f_i(t')}{f_i(t)}\frac{\dot{f}_{\rm coll,g}}{f_{\rm coll,g}}\left(\frac{1+z'}{1+z}\right)^{\alpha+1} \times \int_{\nu'_{\rm min}}^{\infty} d\nu' \nu'^{-\alpha-4} e^{-\tau(R_0,\nu')}\sum_i (\nu'-\nu_i)x_i\sigma_{i0}\nu_i^3. \quad (16)$$

We can estimate the typical energies of the photons that are absorbed close to the source: at $z = 20$, for $\nu \simeq 100$ eV, the photon is absorbed at a comoving distance $\simeq$3 Mpc from the source, while a photon of 1 keV is absorbed at $\simeq$300 Mpc. Therefore, the low-energy photons are absorbed locally and determine the heating profile of the near zone, while the high-energy photons play the role of determining the evolution of the average temperature, which we discuss next. One can compute the optical depth of the high-energy photons to determine the fraction of these photons that is absorbed until the epoch of interest; for $\nu = 2$ keV, nearly 80% of the photons emitted at $z = 20$ remain unabsorbed at $z = 15$. This means that some of these photons are not absorbed locally and they also do not participate in heating in the far zone; we return to this point in the next subsection. We also note that X-ray photons are not absorbed within the H II region; hence, the effective length for computing the optical depth is not R_0 but $R_0 - R_x$, which we take into account in our numerical computation.

2.2.2. Far Zone

In the far zone, multiple sources contribute to the heating at any point. As noted above, low-frequency X-ray photons are preferentially absorbed close to the ionizing region in the near zone (Equation (8)), while higher-frequency photons escape far away from the ionizing centers and contribute to global heating. This can be simplified when the distance traveled by the photon before being absorbed exceeds the mean distance between sources. As the comoving mean distance between sources is on the order of 1 Mpc at $z \simeq 20$ for many of the models we consider, it is a good approximation for our study.

In calculating the far-zone temperature, we essentially take into account all the X-ray frequencies emitted by all the sources since the time they were turned on. To calculate the increase in temperature due to all faraway sources, we choose a random point and calculate the increase in temperature at that point due to sources that lie in a shell of thickness dR_0 at a distance R_0, and then we integrate it over all R_0. We can take the upper limit of R_0 to correspond to the redshift of star formation $R_{\rm final} = R_0(z_\star)$. If we take the minimum value of R_0 to be 0, we get the total (average) temperature increase due to all sources over the history of the universe.

Using the global ionization fraction for the redshift of the chosen shell $f_i(z(R_0))$, the volume of ionized gas inside this shell at a comoving distance R_0 is $4\pi R_0^2 dR_0 f_i(z(R_0))$. Therefore, we can compute the impact of distant sources by replacing $4\pi/3R_x^3$ in Equation (16) with $4\pi R_0^2 dR_0 f_i(z(R_0))$ and integrating over R_0. This gives us

$$\Delta T'_{\rm bg} = \frac{hf_{\rm H}\alpha N_{\rm heat} f_\star n_0 \nu_{\rm min}^\alpha}{k_B\zeta}(1+z_0')^2 \times \int_0^{R_0(z_\star)} dR_0 \int_{t(z_\star)}^{t(z)} dt' \frac{\dot{f}_{\rm coll,g}(t')}{f_{\rm coll,g}(t')} f_i(t')\left(\frac{1+z'}{1+z}\right)^{\alpha+1} \times \int_{\nu'_{\rm min}}^{\infty} d\nu' \nu'^{-\alpha-4} e^{-\tau(R_0,\nu')}\sum_i (\nu'-\nu_i)x_i\sigma_{i0}\nu_i^3. \quad (17)$$

2.2.3. Overlap

During the initial phase of the evolution of the heated bubbles, when the ionized and partially heated fractions (f_i and f_h, respectively) are small, the partially heated fraction grows, and so does the background temperature. At low redshift, the heating bubbles will expand and start to overlap. In this subsection, we discuss how we take into account the impact of these overlaps. Defining the ionization volume fraction

$$f_i = \sum_{R_x} \frac{4\pi}{3} N(R_x) R_x^3, \quad (18)$$

where R_x are the radii of the ionization bubbles and $N(R_x)$ is the number density of the bubbles with an ionization radius R_x. Similarly, we can define the volume fraction due to the heating bubbles to be

$$f_{hb} = \sum_{R_x} \frac{4\pi}{3} N(R_x)(R_h^3 - R_x^3). \quad (19)$$

This quantity can exceed unity due to significant overlap as the universe evolves. Therefore, we define another quantity, f_h, that corresponds to the actual volume fraction occupied by the heating bubbles. This can be derived by recognizing that, in the case of overlap, within every heating bubble, there can be part of another heating bubble or ionization bubble:

$$f_h = \sum_{R_x} \frac{4\pi}{3} N(R_x)(R_h^3 - R_x^3)(1 - f_i - f_h) = f_{hb}(1 - f_i - f_h).$$

This gives us

$$f_h = \frac{f_{hb}(1-f_i)}{1+f_{hb}}.$$

Here f_h remains less than unity even if the value of f_{hb} becomes much larger than unity and approaches f_{hb} when the heating and ionization fractions are small. This allows us to successfully model the overlap of the heating bubbles.

Also, since the bubbles overlap, the temperature of a profile around an ionizing source should contain a contribution due to other overlapping bubbles:

$$T_p = T_s + T_o. \tag{20}$$

Here T_p, the resultant temperature, is the sum of T_s, the temperature due a nearby source, and T_o, the average contribution due to overlap. We recursively define T_o as

$$\begin{aligned} T_o &= \sum_{R_x} \sum_{s} f_s (T_s + T_o) \\ &= \sum_{R_x} \sum_{s} \frac{4\pi}{3} N(R_x) \frac{f_h}{f_{hb}} ((R_s + \Delta R_s)^3 - R_s^3) T_s + f_h T_o \\ &= \frac{1}{1 - f_h} \sum_{R_x} \sum_{s} \frac{4\pi}{3} N(R_x) \frac{f_h}{f_{hb}} ((R_s + \Delta R_s)^3 - R_s^3) T_s, \end{aligned} \tag{21}$$

where R_x and R_h are the radii of the chosen ionization bubble and the outer radius of the corresponding heating bubble, respectively, and R_s and ΔR_s are the inner radius of the shell with a temperature s around the chosen bubble and the thickness of this shell, respectively. We add T_o to the fluctuations but subtract T_o/f_n from the background to maintain the energy budget.

2.2.4. Modeling

Equations (16) and (17) can be used to compute the temperature profile for a single self-ionized region and the evolution of global heating.

We use the following prescription for defining the near and far zones. The radius of the near zone is defined as the distance at which the temperature increase due to that source (over its history) is less than 1 K. The temperature in the far zone depends on the choice of minimum R_0 in Equation (17). We choose $R_0 = 0$, which means the photon energy absorbed in the near zone is also included. However, as we can independently estimate the total amount of energy absorbed in the near zone, we subtract this energy from the energy budget used to estimate the far-zone temperature. The far-zone temperature is then added to the temperature profile of the near zone to consistently take into account the fact that Equation (17) gives the global temperature at all points, including the near zone.

We note that while the definition of the radius of the locally heated region is somewhat arbitrary, its impact on the breakup of the energy budget is negligible. Also, and importantly, the correlation functions as defined in the next sections are minimally affected by this definition, as the correlation functions depend only upon the gradient of temperature.

We explore three parameters to model heating in this paper.

1. α: X-ray spectrum power index. We take three possible values, 1.0, 1.5, and 2.0, with the middle value to be the standard case. For a higher value of α, there are more photons at a low frequency. These photons more effectively heat up the medium, since there is a higher probability of them being absorbed. Therefore, with higher α, the background temperature is high, and the heating profiles are steeper.

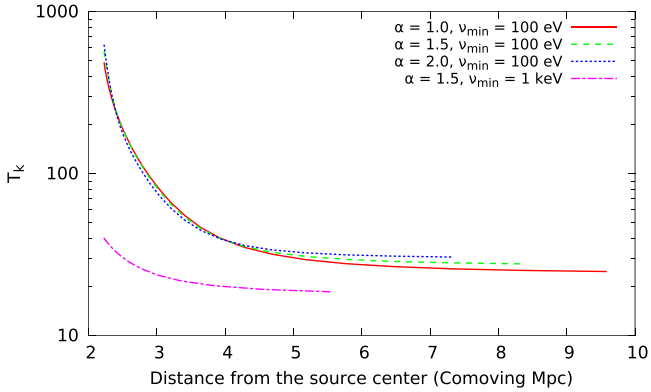

Figure 3. Heating profiles around a bubble at $z = 17$ for various values of α and $\nu_{\rm min}$ with $\zeta = 10$ and $N_{\rm heat} = 1.0$. It is seen that for $\nu_{\rm min} > 1$ keV, the temperature is smaller and the profile around a source is shallow, or there is less distinction between the near and far zones (for details, see text).

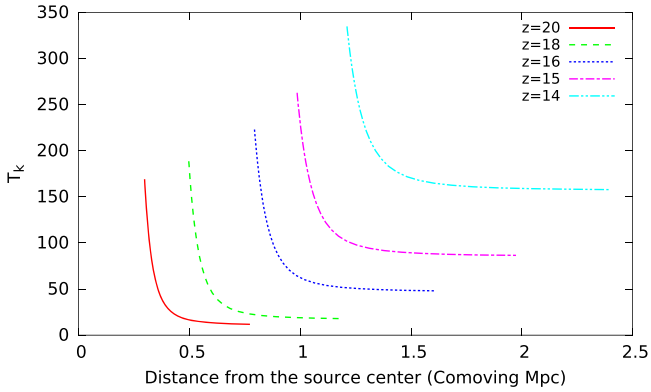

Figure 4. Evolution of the heating profile around an ionized bubble for $\alpha = 1.5$, $\nu_{\rm min} = 100$ eV, $\zeta = 10$, and $N_{\rm heat} = 1.0$. The size of the fiducial ionized bubble is assumed to grow as the mean ionized fraction in the universe. The smallest radius in each profile displayed is the size of the ionized region. The profiles shown reflect the growth of the mean ionization fraction and the increase in the background temperature.

2. $N_{\rm heat}$: number of X-ray photons emitted per stellar baryon. For our study, we assume $N_{\rm heat}$ in the range 0.1–10.0.
3. $\nu_{\rm min}$: minimum X-ray frequency escaping the source halo. We take two possible values, 100 eV and 1 keV. For a given $N_{\rm heat}$, a higher value of $\nu_{\rm min}$ means the emitted photons are more energetic. They free-stream into the medium and uniformly heat the medium with little fluctuations around source halos.

To explore more complicated models, where the X-ray luminosity is not a power law (e.g., Fialkov et al. 2014), we can take $N_{\rm heat}$ and α to be a function of frequency ν and time. However, we do not explore such models in this paper.

In Figure 3, we plot temperature profiles around an ionization bubble at $z = 17$ for $\zeta = 10$, $N_{\rm heat} = 1.0$, and three values of α. The figure also displays a case when $\nu_{\rm min} = 1$ keV. In this case, owing to the absence of low-energy photons, the near-zone profile around the source is very shallow. Also, as noted above, the heating is suppressed in this case even in the far zone, as many high-energy photons remain unabsorbed (Fialkov et al. 2014). In Figure 4, we show the evolution of the heating profile around an ionized bubble (similar results have been obtained by, e.g., Venkatesan & Benson 2011; Ghara et al. 2015). This figure captures the

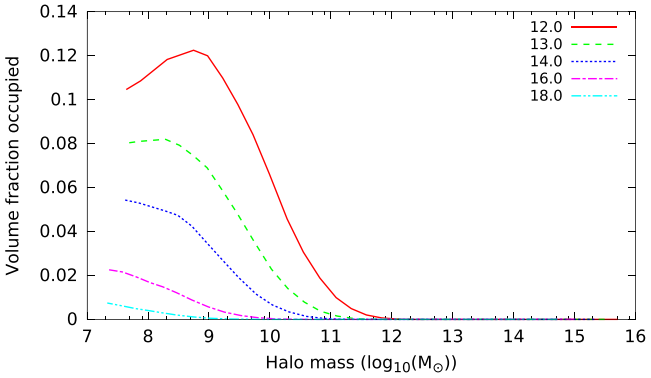

Figure 5. Evolution of the size distribution of the heated regions (see text for details) as a function of halo mass for $\zeta = 10$, $\alpha = 1.5$, and $N_{\rm heat} = 1$.

impact of the growth of the ionized region and average ionization fraction on the heating profile and background temperature. In Figure 5, we show the heating bubble size distribution corresponding to the ionization bubbles from Figure 2.

2.3. Lyα Radiation

As noted in Section 2, Lyα radiation plays an important role in determining the brightness temperature of H I emission from the EoR. For EoR studies, all the radiation between Lyα and the Lyman limit is referred to as Lyα, and we shall follow this convention. Photons in this frequency band are not absorbed in the H II region but escape into the surrounding medium and redshift until the frequency nearly equals the resonant frequency of one of the Lyman series lines. Given the complicated frequency structure of Lyman series lines, these photons are absorbed at varying distances from the source. Our aim here is to determine the conditions under which this radiation couples the spin temperature of the H I line T_S to the matter kinetic temperature T_K. This coupling depends on two factors: the region of influence of the Lyα radiation and the coupling coefficient y_α (Equation (1)).

First, we find the Lyα influence region, which is mainly determined by the distance traveled by the Lyβ photons to redshift to Lyα frequency. If these photons were emitted at $z = z_e$ and absorbed at $z = z_a$ with $\nu_e = \nu_\beta$ and $\nu_a = \nu_\alpha$, then the comoving distance traveled by the photon before it is absorbed in an expanding universe is

$$R_{\rm max} \simeq \frac{1422\ \ {\rm Mpc}}{(1+z_e)^{1/2}}.$$

We note that $R_{\rm max}$ is much larger than the mean distance between ionization bubbles at any redshift. For $\zeta = 15$, the values of the mean comoving distance between the bubbles for redshifts 25, 20, and 15 are 9.66, 2.61, and 1.08 Mpc, respectively. Therefore, the Lyα regions are very large and merge very early. However, this would create a homogeneous coupling to H I atoms only if y_α is high enough (Equation (1)).

The Lyα coupling coefficient, y_α, is a function of the Lyα photon (physical) number density, n'_α (Field 1958; Chen & Miralda-Escudé 2004):

$$y_\alpha = 5.9 \times 10^{11} \frac{n'_\alpha}{T_K^{3/2}}. \quad (22)$$

For efficient coupling between the kinetic temperature T_K and spin temperature T_S, we need $y_\alpha \gtrsim T_{\rm CMB}/T_K$.

We assume that the Lyα contribution comes through two main factors: Lyα emitted from the sources and Lyα created due to X-ray photoelectrons (Venkatesan et al. 2001). The latter is generally negligible. To calculate the number density of Lyα photons from ionizing sources, we use the same method applied in the previous section, which seeks to express the Lyα photon luminosity in terms of the radii of ionizing regions. This method allows us to compute both the near- and far-zone contributions from Lyα photons. In this paper, we compute only the far-zone contribution, which comes from photons between Lyα and Lyβ. Assuming a flat spectrum between Lyα and Lyβ, the number density of Lyα photons at a comoving distance R_0 from the source is

$$n'_{\alpha,\star} = \frac{\dot{N}_\alpha}{4\pi c R_0^2} \frac{2\Delta\nu_\alpha}{\nu_\beta - \nu_\alpha} \frac{(1+z')^3}{1+z}.$$

Here $\dot{N}_\alpha$ is the Lyα luminosity of a given halo, and $\Delta\nu_\alpha = \sqrt{8kT\ln(2)/m_p c^2}\,\nu_\alpha$ is the Doppler line width. This factor arises because at the source, the photons are emitted with frequencies between ν_β and ν_α, but the only frequencies that are absorbed at redshift z' are in the range of $\Delta\nu_\alpha$ around ν_α.

The Lyα luminosity, $\dot{N}_\alpha$, can be expressed in terms of the size of the ionization halo, assuming that the Lyα luminosity scales with the ionizing luminosity with a factor f_L and the balance between ionization and recombination in the ionizing region:

$$\dot{N}_\alpha = f_L \frac{4\pi}{3} n_0^2 \alpha_B C R_x^3 (1+z)^3.$$

Here $10 < f_L < 100$ (e.g., Chen & Miralda-Escudé 2004).

We can calculate the Lyα number density due to faraway sources in the same way as described in the previous section. In a thin shell of width dR_0 at a comoving distance R_0 from the receiving point, the contributing ionization fraction is $4\pi R_0^2 dR_0 f_i(z)$. Therefore, we integrate over R_0. Here we take the lower limit of the integral $R_0 = 0$, while the upper limit is given by the Lyα influence region:

$$\begin{aligned} n'_{\alpha,{\rm bg}} &= \frac{f_L n_0^2 \alpha_B C}{c} \int_0^{R_{\rm max}} dR_0 f_i(z) \frac{2\Delta\nu_\alpha}{\nu_\beta - \nu_\alpha} (1+z')^3 (1+z)^2 \\ &= 4.71 \frac{f_L n_0^2 \alpha_B C}{c^2} \sqrt{\frac{k}{m_p}} \frac{\nu_\alpha}{\nu_\beta - \nu_\alpha} (1+z')^3 \\ &\quad \times \int_0^{R_{\rm max}} dR_0 f_i(z) T_K(z)^{1/2} (1+z)^2. \end{aligned} \quad (23)$$

Here $R_{\rm max}$ is the distance corresponding to $z_{\rm max} = (1+z')(\nu_\beta/\nu_\alpha) - 1$.

From Equation (1), it follows that for $q \equiv y_\alpha T_{\rm K}/T_{\rm CMB} \geqslant 1$, we expect the spin temperature to relax to the matter temperature T_K. Using Equations (22) and (23), we can compute y_α. Given the complicated temperature structure of the regions outside the ionized region, q can vary substantially as it scales as $T_K^{-1/2}$. We find that for all the models we consider here, q exceeds unity for $z < 20$; e.g., for $\zeta = 10$, $\alpha = 1.5$, $N_{\rm heat} = 0.5$, $f_L = 100$, $C = 2$, and $z = 20$, the background temperature is 9.1 K, the value of y_α is 40, and $q = 6.3$.

Here we do not calculate the effect of higher-order Lyman transitions (e.g., from Lyγ to Lyβ), since their total number density is less than that of the photons between Lyβ and Lyα. Moreover, they will be absorbed closer to the source.

3. Autocorrelation of Brightness Temperature T_b

The autocorrelation of ψ (Equation (3)) can be defined as

$$\begin{aligned}\mu &= \langle\psi_1\psi_2\rangle - \langle\psi\rangle^2 \\ &= \langle n_1(1+\delta_1)(1-s_1)n_2(1+\delta_2)(1-s_2)\rangle \\ &\quad - \langle n_1(1+\delta_1)(1-s_1)\rangle^2. \end{aligned} \tag{24}$$

Here n_1, δ_1, and s_1 are the values of ionization, overdensity, and heating ($T_{\rm CMB}/T_S$) at point 1 ($\boldsymbol{r}_1$). Similarly, n_2, δ_2, and s_2 are values at point 2 ($\boldsymbol{r}_2$). It should be noted that the autocorrelation function μ is a function of $r = |\boldsymbol{r}_2 - \boldsymbol{r}_1|$, as the process of reionization is statistically homogeneous and isotropic. To calculate μ, we need to find all the pairs of points that are separated by a distance r and average them over the entire space. To compute the correlation function, we use geometric arguments to find the probability of pairs with given values and take their weighed average.

Equation (24) can be greatly simplified if we assume that density has no correlation with ionization or heating ($\eta = \langle n\delta\rangle = 0$ and $\langle s\delta\rangle = 0$). In this work, we make the assumption that cross-correlation between ionization and density, as well as between heating and density, is subdominant. We expect a positive correlation between ionization and density, since dense regions collapse and get ionized first. Using excursion set formalism, Furlanetto et al. (2004a) computed this cross-correlation and showed that it is generally subdominant as compared to autocorrelation terms (Figure 5 of their paper). The correlation of heating with density is also expected to be positive, as the dense regions surrounding ionization bubbles should have larger temperatures. However, on the scale of heated regions, the density correlation is smaller at high redshifts. Simulations show that the density-heating cross-correlation is subdominant (Ghara et al. 2015) as compared to other contributions. This gives us

$$\begin{aligned}&\langle n_1 n_2(1+\delta_1+\delta_2+\delta_1\delta_2)(1-s_1-s_2+s_1s_2)\rangle \\ &\quad = (1+\xi)\langle n_1 n_2(1-s_1-s_2+s_1s_2)\rangle,\end{aligned}$$

where $\xi = \langle\delta(\boldsymbol{r}_1)\delta(\boldsymbol{r}_2)\rangle$ is the autocorrelation function of the H I density perturbation; we compute ξ using the ΛCDM model power spectrum, assuming the relative bias between the dark matter and the H I, $b = 1$. And,

$$\begin{aligned}\langle n_1(1+\delta_1)(1-s_1)\rangle &= \langle 1+\delta_1\rangle\langle n_1(1-s_1)\rangle \\ &= \quad f_n - \langle n_1 s_1\rangle,\end{aligned}$$

since $\langle\delta\rangle = 0$ and $f_n = \langle n\rangle$ is defined as the dimensionless average neutral volume fraction at that redshift. This finally yields

$$\begin{aligned}\mu &= (1+\xi)(\langle n_1 n_2\rangle - \langle n_1 n_2 s_1\rangle - \langle n_1 n_2 s_2\rangle \\ &\quad + \langle n_1 n_2 s_1 s_2\rangle) - (f_n - \langle n_1 s_1\rangle)^2.\end{aligned}$$

We can greatly simplify correlation functions higher than second order. Let us first consider $\langle n_1 n_2 s_1\rangle$. This corresponds to the joint probability that the point $\boldsymbol{r} = \boldsymbol{r}_1$ is both neutral and heated to a temperature such that $s = s_1$, while the second point is neutral. As noted above, n can be either unity (neutral point) or zero (ionized point), while s can take any arbitrary value depending on the kinetic temperature. However, in our model, $T_K \gg T_{\rm CMB}$ if and only if that point is ionized ($T_K \sim 10^4$ K). In other words, for a point $s = 0$ if and only if that point has $n = 0$. Therefore, the condition of point 1 being neutral ($n_1 = 1$) is fulfilled by it being not heated to a very high temperature ($s_1 \neq 0$). This allows us to simplify higher point correlation functions as

$$\begin{aligned}\langle n_1 n_2 s_1\rangle &= \langle n_2 s_1\rangle \\ \langle n_1 n_2 s_2\rangle &= \langle n_1 s_2\rangle \\ \langle n_1 n_2 s_1 s_2\rangle &= \langle s_1 s_2\rangle.\end{aligned}$$

And, since we choose two points randomly, we also have

$$\langle n_1 s_2\rangle = \langle n_2 s_1\rangle.$$

Finally, we have

$$\mu = (1+\xi)(\langle n_1 n_2\rangle - 2\langle n_1 s_2\rangle + \langle s_1 s_2\rangle) - (f_n - \langle n_1 s_1\rangle)^2. \tag{25}$$

Here we have introduced cross-correlations between kinetic temperature (heating) and ionization ($\langle n_1 s_2\rangle$) and autocorrelation of heating ($\langle s_1 s_2\rangle$). These terms have a significant effect in brightness temperature correlation. As noted above, all the two-point correlations are functions of the distance between two points $|\boldsymbol{r}_2 - \boldsymbol{r}_1|$.

In the following subsections, we explore certain simplifying cases and limits.

3.1. Simplifying Cases

3.1.1. Uniform Heating

As a simplifying case, we examine a model where there is uniform heating outside the ionized bubbles, and all the neutral gas of the IGM is at a uniform temperature of $T_{\rm bg}$:

$$\psi = n(1+\delta)(1-s_b).$$

The correlation is

$$\begin{aligned}\mu &= (1-s_b)^2\langle n_1(1+\delta_1)n_2(1+\delta_2)\rangle \\ &\quad - (1-s_b)^2\langle n_1(1+\delta_1)\rangle^2 \\ &= (1-s_b)^2((1+\xi)\langle n_1 n_2\rangle - f_n^2).\end{aligned} \tag{26}$$

Here $s_b = T_{\rm CMB}/T_{\rm bg}$. At early times, $T_{\rm bg}$ can approach the adiabatically cooled temperature of the IGM gas, which is smaller than $T_{\rm CMB}$. If the ionization fraction is too small, $\langle n_1 n_2\rangle \simeq f_n^2 \simeq 1$. This gives us

$$\mu = \xi(1-s_b)^2.$$

At late times, $T_{\rm bg} \gg T_{\rm CMB}$ owing to X-ray heating, driving s_b to zero, which gives

$$\mu = -f_n^2 + (1+\xi)\langle n_1 n_2\rangle. \tag{27}$$

This result is consistent with Zaldarriaga et al. (2004).

3.1.2. Correlation at Very Large and Small Scales

We can compute the small- and large-scale limits of the correlation function given by Equation (25) under fairly general conditions. Both ionization and heating inhomogeneities are caused by bubbles of a given size distribution, which determine the scales of correlation. As discussed in the foregoing, the size distribution evolves, and bubbles could have complicated profiles. However, for scales greater than the largest bubbles, the correlation function owing to the ionization and heating inhomogeneities vanishes, and the H I correlation function is determined by only density perturbations. In this limit, we get

$$\begin{aligned}\langle n_1 n_2\rangle &= \langle n_1\rangle\langle n_2\rangle = f_n^2\\ \langle n_1 s_2\rangle &= \langle n_1\rangle\langle s_2\rangle = f_n\langle s\rangle\\ \langle s_1 s_2\rangle &= \langle s_1\rangle\langle s_2\rangle = \langle s\rangle^2.\end{aligned}$$

Therefore,

$$\begin{aligned}\mu &= (1+\xi)(\langle n_1 n_2\rangle - 2\langle n_1 s_2\rangle + \langle s_1 s_2\rangle) - (f_n - \langle n_1 s_1\rangle)^2\\ &= (1+\xi)(f_n - \langle s\rangle)^2 - (f_n - \langle s\rangle)^2\\ &= \xi(f_n - \langle s\rangle)^2. \end{aligned} \quad (28)$$

In this limit, the correlation function scales as the density correlation function ξ. We also note that the correlation function vanishes when $f_n = \langle s\rangle$ (close to the global heating transition).

In the small-scale limit ($\boldsymbol{r}_2 = \boldsymbol{r}_1$), we get

$$\begin{aligned}\mu &= (1+\xi_0)(\langle n_1 n_1\rangle - 2\langle n_1 s_1\rangle + \langle s_1 s_1\rangle) - (f_n - \langle n_1 s_1\rangle)^2\\ &= (1+\xi_0)(f_n - 2\langle s\rangle + \langle s^2\rangle) - (f_n^2 - 2f_n\langle s\rangle + \langle s\rangle^2).\end{aligned} \quad (29)$$

Here $\xi_0 = \xi(0)$, or the correlation function computed at zero lag, which equals the rms of the density perturbations. Since Equation (29) gives an rms, it is always positive.

We verify Equations (28) and (29) as the large- and small-scale limits of the H I correlation function computed using the methods described in the next sections.

3.2. Modeling and Notations

Our aim in this paper is to analytically model the early phase of the EoR. This issue can essentially be reduced to computing the autocorrelation of the neutral fraction $\langle n_1 n_2\rangle$, the ionization-heating cross-correlation $\langle s_1 n_2\rangle$, and the heating autocorrelation function $\langle s_1 s_2\rangle$. We make several assumptions to make this problem analytically tractable. The main assumption is that for a given self-ionized region, the heating and ionization bubbles are spherical and concentric and the ionization centers are uncorrelated. Each self-ionized and heating region can be treated as isolated, so long as both the ionization and heating fractions are small, which is expected during the early phase of reionization. As discussed in Section 2.2, X-ray heating can be split into near- and far-zone effects. While the near-zone effects are owing to the vicinity of a self-ionized region, the far-zone effects take into account the impact of all the sources and their evolution. We model them both in this paper. An additional complication in the case of heating is that near-zone heating has a smooth profile around it, as opposed to ionized bubbles, which have uniform ionization within the bubble with a sharp boundary. We explicitly account for the heating rate as a function of distance from the source and its smooth merger into the background. In Figure 6, we show the geometry of the self-ionized region and the heating zone beyond it. To compute the correlations, we assume two random points separated by a distance r as shown in Figure 7. The formalism used for the

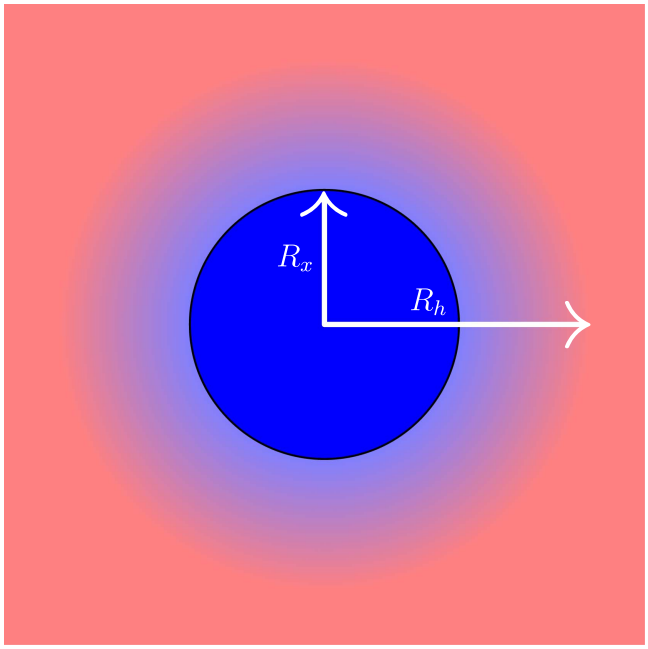

Figure 6. Topology of the ionized and heated regions typical of the partially heated universe. The ionized region of size R_x (with a sharp boundary) is seen to be surrounded by a heated fuzzy region of radius R_h. The color scheme shows the temperature, T; $T \simeq 10^4$ in the ionized regions and is much smaller in the heated region. It falls with distance from the source center and smoothly merges with the background.

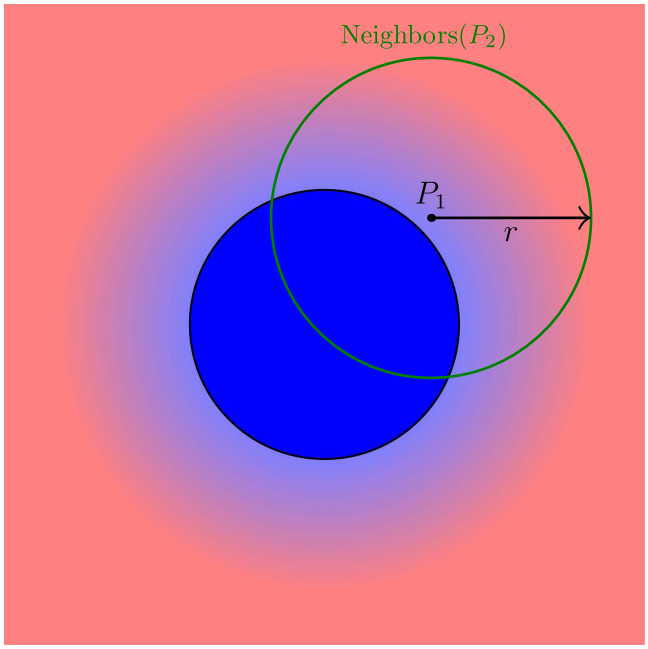

Figure 7. Randomly choosing a point and finding a correlation with its neighbor at a distance r.

Table 1
Notations

Symbols	Explanation
δ	Overdensity of H I gas
n	Ionization state of H I gas; neutral means $n = 1$ and ionized means $n = 0$
s	Temperature state defined as $s = T_{\rm CMB}/T_S$
ψ	Dimensionless brightness temperature: $\psi = n(1 + \delta)(1 - s)$
ξ	Autocorrelation of overdensity δ: $\xi = \langle\delta_1\delta_2\rangle$
μ	Autocorrelation of dimensionless brightness temperature ψ: $\mu = \langle\psi_1\psi_2\rangle - \langle\psi\rangle^2$
f_i	Average ionized volume fraction
f_n	Average neutral volume fraction
f_{hb}	Total volume fraction due to heating bubbles (without taking into account the overlaps)
f_h	Average heated volume fraction after taking into account the overlaps
f_b	Average background volume fraction
R_x	Radius of the given ionization bubble
R_h	Outer radius of the given heating bubble, $R_h = R_h(R_x)$
R_s	Inner radius of the shell with temperature s around the given bubble
ΔR_s	Thickness of the shell with temperature s around the given bubble
$N(R_x)$	Number density of ionization bubbles of radius R_x
$P(n_p)$	Probability of point p being neutral
$P(\widetilde{n_p})$	Probability of point p being ionized
$P(\widetilde{n_p}(R_x))$	Probability that point p belongs to an ionization bubble of radius R_x
$P(s)$	Probability that the given point has a temperature s
$P(s_b)$	Probability that the given point is in the background
$P(s, R_x)$	Probability that the given point has a temperature s and lies in the bubble of ionization radius R_x

computation of the correlation functions is described in Appendix B.

We assume that at a given z, the ionized bubbles have various radii R_x. The number density of the bubbles of radius R_x is $N(R_x)$. Between R_x and R_h, the outer boundary of the heating bubble (Figure 6), we take shells of thickness $\Delta R(R_x, s)$ having a nonzero temperature $s = T_{\rm CMB}/T_S$. A detailed description of the notations followed in this paper given in Table 1.

If the point is randomly chosen,

$$P(\tilde{n}(R_x)) = N(R_x)\frac{4\pi}{3}R_x^3$$

$$P(\tilde{n}) = \sum_{R_x} P(\widetilde{n_p}(R_x)) = \sum_{R_x} N(R_x)\frac{4\pi}{3}R_x^3 = f_i$$

$$P(n) = 1 - \sum_{R_x} N(R_x)\frac{4\pi}{3}R_x^3 = f_n$$

$$P(s, R_x) = N(R_x)\frac{4\pi}{3}f_b((R_s + \Delta R_s)^3 - R_s^3)$$

$$P(s) = \sum_{R_x} P(s, R_x).$$

The heated volume fraction can be expressed as

$$f_h = \sum_s \sum_{R_x} P(s, R_x) = \sum_{R_x} N(R_x)\frac{4\pi}{3}f_b(R_h^3 - R_x^3). \quad (30)$$

The background volume fraction is

$$f_b = \frac{1 - f_i}{1 + f_{hb}} = 1 - f_i - f_h$$
$$= 1 - \sum_{R_x} N(R_x)\frac{4\pi}{3}(f_b(R_h^3 - R_x^3) + R_x^3). \quad (31)$$

It should be noted that when f_{hb} is small, f_h approaches f_{hb} and $f_b \simeq 1 - f_i - f_{hb}$, the values expected if the overlap is neglected.

3.3. Complete Model

Our main aim is to calculate ionization and heating correlations for epochs at which the ionization volume fraction is small. This ensures that the ionization bubbles are separate and nonoverlapping. However, as described in Section 2.2, our formulation allows us to deal with the overlap of heating bubbles. We describe in detail our formalism to compute the neutral fraction autocorrelation, neutral fraction-heating cross-correlation, and heating autocorrelation next.

3.3.1. Correlation of Neutral Region ($\langle n_1 n_2\rangle$)

We need to find the probability (fraction) of pairs with both points neutral (outside the ionization bubble):

$$\langle n_1 n_2\rangle = 1^2\, P(n_1 \cap n_2) + 0\, P(n_1 \cap \widetilde{n_2}) + 0\, P(\widetilde{n_1} \cap n_2) + 0\, P(\widetilde{n_1} \cap \widetilde{n_2}) = P(n_1 \cap n_2).$$

Using Equation (53),

$$P(n_1 \cap n_2) = P(n_1) - P(n_1 \cap \widetilde{n_2}).$$

First, we assume that point 2 is ionized. Therefore, it lies in some ionized bubble. The statement that its neighbor (point 1) at a distance r lies in a neutral region means that point 1 lies outside that bubble and also outside any other bubble. Using Equation (52),

$$P(n_1 \cap \widetilde{n_2}) = P((n_1(\text{out same}) \cap n_1(\text{out other})) \cap \widetilde{n_2})$$
$$= P(n_1(\text{out other})|(n_1(\text{out same}) \cap \widetilde{n_2}))$$
$$\times P(n_1(\text{out same}) \cap \widetilde{n_2}).$$

If we assume that the bubbles are uncorrelated and nonoverlapping, then $P(n_1(\text{out other})|(n_1(\text{out same}) \cap \widetilde{n_2}))$ is the probability that point 1 is neutral, given that point 2 lies in some bubble and point 1 lies outside that bubble. This quantity is equal to the average neutral fraction f_n in the present case.[4]

Now we need to find $P(n_1(\text{out same}) \cap \widetilde{n_2})$ = the probability that point 2 is in an ionization bubble and point 1 lies outside of that bubble. Point 2 can be in a bubble with any

[4] If we assume that the bubbles are uncorrelated and randomly distributed, then once a point is outside a certain bubble, its probability of being ionized or neutral is proportional to the global ionized or neutral fractions, respectively. However, this formalism applies because we are assuming an infinite volume. If we had assumed a finite volume (as would be the case for a simulation), the ionized volume fraction around an ionized bubble would be less than the global ionized volume fraction, since we need to take into account the volume occupied by said ionization bubble. For a finite volume, this effect should cause an anticorrelation between the bubbles. Throughout this paper, we assume an infinite volume for averaging.

radius R_x. Therefore,

$$P(n_1(\text{out same}) \cap \widetilde{n_2}) = \sum_{R_x} P(n_1(\text{out same}) \bigcap \widetilde{n_2}(R_x)) = \sum_{R_x} P(\widetilde{n_2}(R_x)) P(n_1(\text{out same}) | \widetilde{n_2}(R_x)) = \sum_{R_x} N(R_x) \frac{4\pi}{3} R_x^3 D(x, R_x),$$

where $P(n_1(\text{out same}) | \widetilde{n_2}(R_x)) = D(x, R_x) =$ the probability that point 1 is outside of the bubble, given that point 2 is inside a bubble of some radius R_x. Therefore,

$$\langle n_1 n_2 \rangle = f_n - f_n \sum_{R_x} N(R_x) \frac{4\pi}{3} R_x^3 D(r, R_x). \tag{32}$$

This expression reduces to the results of Zaldarriaga et al. (2004) when a single scale corresponding to size of ionized bubbles is taken for a fixed ionization fraction. It also follows from our discussion that the scenario envisaged in Figure 6 is valid at an early time.

3.3.2. Correlation between Neutral Region and Heating ($\langle n_1 s_2 \rangle$)

We need to find the correlation between neutral points and points with $s \neq 0$:

$$\langle n_1 s_2 \rangle = s_b P(n_1 \bigcap s_b) + \sum_{0<s<s_b} s P(n_1 \bigcap s). \tag{33}$$

Here s_b corresponds to the background (far zone) temperature at any redshift. The first term can be written as

$$P(n_1 \cap s_b) = P(s_b) - P(s_b \cap \widetilde{n_1}).$$

We apply the procedure followed in the previous section. As point 1 is ionized, it lies in some ionization bubble. The statement that its neighbor (point 2) at a distance r lies in the background region means that point 2 lies outside the heating bubble corresponding to that ionization bubble and outside any other heating bubble:

$$P(s_b \cap \widetilde{n_1}) = P(s_2(\text{out other}) | (s_2(\text{out same}) \cap \widetilde{n_1})) \times P(s_2(\text{out same}) \cap \widetilde{n_1}).$$

As the bubbles are assumed to be nonoverlapping and uncorrelated, $P(s_b(\text{out other}) | (s_b(\text{out same}) \cap \widetilde{n_1}))$ gives the probability that point 2 is in the background region, given that point 1 lies in some ionization bubble and point 2 lies outside the heating bubble corresponding to that ionization bubble. This probability equals the fraction of the universe heated at a background temperature f_b (see footnote 2).

Our next task is to compute $P(s_2(\text{out same}) \cap \widetilde{n_1})$, which is the probability of point 1 being in an ionization bubble and point 2 being out of the heating bubble corresponding to that ionization bubble. Given the distribution of radii of the ionization bubbles, R_x, we have

$$P(s_2(\text{out same}) \cap \widetilde{n_1}) = \sum_{R_x} N(R_x) \frac{4\pi}{3} R_x^3 P(s_2(\text{out same}) | \widetilde{n_1}(R_x)).$$

We see that $P(s_2(\text{out same}) | \widetilde{n_1}(R_x)) = E(r, R_x, R_h(R_x))$, the probability that point 2 is outside of the heating bubble corresponding to the ionization bubble of radius R_x in which point 1 lies. Thus, we have

$$P(n_1 \bigcap s_b) = f_b - f_b \sum_{R_x} N(R_x) \frac{4\pi}{3} R_x^3 E(r, R_x, R_h(R_x)). \tag{34}$$

We also note that, in the limit $R_h \to R_x$, $E(r, R_x, R_h) \to D(r, R_x)$, which allows us to take the limit in which the region outside the ionizing bubbles is uniformly heated.

Now we need to find $P(n_1 \cap s)$, where $0 < s < s_b$. Here point 2 is inside a heating bubble but outside an ionization bubble. Point 2 can be in a heating bubble of any radius; thus,

$$P(n_1 \bigcap s) = \sum_{R_x} P(s, R_x) P(n_1 | s(R_x)),$$

where $P(n_1 | s(R_x))$ is the probability that point 1 is in some neutral region, given that point 2 is in the partially heated region of an ionization bubble of size R_x with $s_2 = s$. If it is outside that ionization bubble, then its probability to be neutral = (1 - the probability of that point being inside an ionization bubble). Using the result of Section 3.3.1,

$$P(n_1 | s(R_x)) = \left(1 - \sum_{R_x'} N(R_x') \frac{4\pi}{3} R_x'^3 D(r, R_x')\right) \times C(r, R_s, R_s + \Delta R_s, R_x),$$

where $C(r, P, Q, R)$, as discussed in Appendix B.3, gives the probability that if point 1 is between radii P and Q from the center of a sphere, then its neighbor point 2 at a distance r is outside a radius R of the same sphere. Therefore,

$$P(n_1 \cap s) = \sum_{R_x} N(R_x) \frac{4\pi}{3} f_b ((R_s + \Delta R_s)^3 - R_s^3) \times \left(1 - \sum_{R_x'} N(R_x') \frac{4\pi}{3} R_x'^3 D(r, R_x')\right) \times C(r, R_s, R_s + \Delta R_s, R_x). \tag{35}$$

This gives us the final expression:

$$\langle n_1 s_2 \rangle = s_b f_b - s_b f_b \sum_{R_x} N(R_x) \frac{4\pi}{3} R_x^3 E(r, R_x, R_h) + \left(1 - \sum_{R_x'} N(R_x') \frac{4\pi}{3} R_x'^3 D(r, R_x')\right) f_b \sum_{R_x} N(R_x) \times \frac{4\pi}{3} \sum_{s(R_x)} s ((R_s + \Delta R_s)^3 - R_s^3) \times C(r, R_s, R_s + \Delta R_s, R_x). \tag{36}$$

In writing Equation (36), we have suppressed the dependence of R_h and R_s on R_x.

We also need to calculate the correlation between ionization and heating at the same point ($\langle n_1 s_1 \rangle = \langle s \rangle$). The signal will be

nonzero only if the chosen point is neutral. Therefore,

$$\langle n_1 s_1 \rangle = s_b f_b + f_b \sum_{R_x} N(R_x) \frac{4\pi}{3} \sum_{s(R_x)} \times s\,((R_s + \Delta R_s)^3 - R_s^3). \quad (37)$$

This quantity can also be represented as the global average of s, as $s = 0$ where $n = 0$.

3.3.3. Correlation of Heating ($\langle s_1 s_2 \rangle$)

The signal will be nonzero only if neither of the points are completely heated or, equivalently, both the points lie outside the ionized regions. Therefore, $s_1 \neq 0$ and $s_2 \neq 0$:

$$\begin{aligned}\langle s_1 s_2 \rangle = {} & s_b^2 P((s_1 = s_b) \cap (s_2 = s_b)) \\ & + 2 s_b \sum_{0<s<s_b} s P((s_1 = s_b) \cap (s_2 = s)) \\ & + \sum_{0<s_p<s_b} \sum_{0<s_q<s_b} s_p s_q P((s_1 = s_p) \cap (s_2 = s_q)). \end{aligned} \quad (38)$$

Following the logic of Section 3.3.1,

$$P((s_1 = s_b) \cap (s_2 = s_b)) = P(s_b) - P((s_1 = s_b) \cap (s_2 = \widetilde{s_b})).$$

If point 2 is not in the background region, it can be in the ionized or heated profile region. In any case, its neighbor point 1 will be in the background region only if it is outside the heated region of the bubble in which point 2 is. Therefore,

$$\begin{aligned} & P((s_1 = s_b) \cap (s_2 = s_b)) \\ & = f_b - f_b \sum_{R_x} N(R_x) \frac{4\pi}{3} ((R_h^3 - R_x^3) \\ & \quad \times f_b C(r, R_x, R_h, R_h) + R_x^3 E(r, R_x, R_h)). \end{aligned} \quad (39)$$

We have

$$\begin{aligned} P((s_1 = s_b) \cap (s_2 = s)) = {} & P(s_1(\text{out other}) | (s_1(\text{out same}) \\ & \times \cap (s_2 = s))) P(s_1(\text{out same}) \cap (s_2 = s)), \end{aligned}$$

where $P(s_1(\text{out other}) | (s_1(\text{out same}) \cap (s_2 = s)))$ is the probability that point 1 is in the background region, given that point 2 is partially heated with a temperature s and point 1 is not inside the bubble in which point 2 is. This probability equals the fraction of the universe heated to a background temperature, f_b (see footnote 2). Here $P(s_1(\text{out same}) \cap (s_2 = s))$ is the probability that point 1 is out of the bubble in which point 2 is, and point 2 is partially heated with a temperature s. As point 2 can be in a bubble with any ionization radius R_x, we have

$$\begin{aligned} & P(s_1(\text{out same}) \cap (s_2 = s)) \\ & = \sum_{R_x} N(R_x) \frac{4\pi}{3} f_b ((R_s + \Delta R_s)^3 - R_s^3) \\ & \quad \times P(s_1(\text{out same}) | (s_2 = s)(R_x)). \end{aligned}$$

Here $P(s_1(\text{out same}) | (s_2 = s)(R_x)) =$ is the probability that point 1 is out of the bubble that has an ionization radius R_x and contains point 2 with temperature s. This equals the probability that point 1 is out of the bubble with an outer radius R_h in which point 2 is located between a radius R_s and $R_s + \Delta R_s$. This gives us

$$\begin{aligned} P((s_1 = s_b) \cap (s_2 = s)) = {} & f_b \sum_{R_x} N(R_x) \\ & \times \frac{4\pi}{3} f_b ((R_s + \Delta R_s)^3 - R_s^3) \\ & \times C(r, R_s, R_s + \Delta R_s, R_h). \end{aligned} \quad (40)$$

In the case where both points are partially heated, these points can belong to the same bubble or different bubbles, which gives

$$P(s_1 \bigcap s_2) = P(s_1 \bigcap s_2(\text{same})) + P(s_1 \bigcap s_2(\text{diff})). \quad (41)$$

Here $P(s_1 \cap s_2(\text{same}))$ is the probability that points 1 and 2 have temperatures s_1 and s_2, respectively, and belong to the same bubble. We calculate $P(s_2(\text{same}) | s_1(R_x))$, which is the probability that if point 1 is located in a bubble with an ionization radius R_x and has a temperature s_1, then point 2 is in the same heating bubble with a temperature s_2. If point 1 is located at a distance between R_{s_1} and $R_{s_1} + \Delta R_{s_1}$ from the center of the sphere, then the fraction of its neighbors at a distance r that are outside the sphere of radius R_{s_2} and inside the sphere of radius $R_{s_2} + \Delta R_{s_2}$ can be computed. However, since bubbles can overlap, point 2 can be neutral or ionized, which leads to

$$\begin{aligned} & P(s_2(\text{same}) | s_1(R_x)) \\ & = (C(r, R_{s_1}, R_{s_1} + \Delta R_{s_1}, R_{s_2}) \\ & \quad - C(r, R_{s_1}, R_{s_1} + \Delta R_{s_1}, R_{s_2} + \Delta R_{s_2})) \\ & \quad \times \left(1 - \sum_{R_x'} N(R_x') \frac{4\pi}{3} R_x'^3 D(r, R_x')\right). \end{aligned}$$

Therefore,

$$\begin{aligned} & \sum_{0<s_1<s_b} \sum_{0<s_2<s_b} s_1 s_2 P(s_1 \cap s_2(\text{same})) \\ & = \sum_{R_x} N(R_x) \frac{4\pi}{3} \sum_{s_1(R_x)} \sum_{s_2(R_x)} \\ & \quad \times s_1 s_2 f_b ((R_{s_1} + \Delta R_{s_1})^3 - R_{s_1}^3) \\ & \quad \times (C(r, R_{s_1}, R_{s_1} + \Delta R_{s_1}, R_{s_2}) \\ & \quad - C(r, R_{s_1}, R_{s_1} + \Delta R_{s_1}, R_{s_2} + \Delta R_{s_2})) \\ & \quad \times \left(1 - \sum_{R_x'} N(R_x') \frac{4\pi}{3} R_x'^3 D(r, R_x')\right). \end{aligned} \quad (42)$$

Now we turn to the second term on the right-hand side of Equation (41). Here $P(s_1 \cap s_2(\text{diff}))$ gives the probability that point 1 has a temperature s_1, point 2 has a temperature s_2, and they both belong to different bubbles. Here we take a simple assumption that if point 2 is outside the bubble in which point 1 is, then its probability of having $s = s_2$ is equal to the global probability of an s_2 temperature shell. Since points 1 and 2 can

belong to bubbles of any size,

$$P(s_1 \cap s_2(\mathrm{diff})) = \sum_{R_x} P(s_1, R_x) C(r, R_{s_1}, R_{s_1} + \Delta R_{s_1}, R_h) \sum_{R_x'} P(s_2, R_x'),$$

which gives us

$$\begin{aligned}
&\sum_{0<s_1<s_b} \sum_{0<s_2<s_b} s_1 s_2 P(s_1 \cap s_2(\mathrm{diff})) \\
&= \sum_{R_x} N(R_x) \frac{4\pi}{3} \sum_{s_1(R_x)} s_1 f_b ((R_{s_1} + \Delta R_{s_1})^3 - R_{s_1}^3) \\
&\times C(r, R_{s_1}, R_{s_1} + \Delta R_{s_1}, R_h) \\
&\times \sum_{R_x'} N(R_x') \frac{4\pi}{3} \sum_{s_2(R_x')} s_2 f_b ((R_{s_2}' + \Delta R_{s_2}')^3 - R_{s_2}'^3). \qquad (43)
\end{aligned}$$

Using Equations (39), (40), (42), and (43), we finally obtain the expression for the heating correlation function:

$$\begin{aligned}
&\langle s_1 s_2 \rangle \\
&= s_b^2 f_b - s_b^2 f_b \sum_{R_x} N(R_x) \frac{4\pi}{3} (f_b (R_h^3 - R_x^3) \\
&\times C(r, R_x, R_h, R_h) + R_x^3 E(r, R_x, R_h)) \\
&+ f_b \sum_{R_x} N(R_x) \frac{4\pi}{3} \sum_{s(R_x)} s((R_s + \Delta R_s)^3 - R_s^3) \\
&\times C(r, R_s, R_s + \Delta R_s, R_h) \\
&\times \left(2 s_b f_b + f_b \sum_{R_x'} N(R_x') \frac{4\pi}{3} \right. \\
&\left. \times \sum_{s'(R_x')} s'((R_{s'}' + \Delta R_{s'}')^3 - R'^3_{s'}) \right) \\
&+ f_b \sum_{R_x} N(R_x) \frac{4\pi}{3} \sum_{s_1(R_x)} \sum_{s_2(R_x)} s_1 s_2 ((R_{s_1} + \Delta R_{s_1})^3 - R_{s_1}^3) \\
&\times (C(r, R_{s_1}, R_{s_1} + \Delta R_{s_1}, R_{s_2}) \\
&- C(r, R_{s_1}, R_{s_1} + \Delta R_{s_1}, R_{s_2} + \Delta R_{s_2})) \\
&\times \left(1 - \sum_{R_x'} N(R_x') \frac{4\pi}{3} R_x'^3 D(r, R_x') \right). \qquad (44)
\end{aligned}$$

We also calculate the correlation of heating at the same point ($\langle s_1 s_1 \rangle = \langle s^2 \rangle$). The signal will be nonzero only if the chosen point is not heated to a very high temperature. Therefore,

$$\langle s_1 s_1 \rangle = s_b^2 f_b + f_b \sum_{R_x} N(R_x) \frac{4\pi}{3} \times \sum_{s(R_x)} s^2 ((R_s + \Delta R_s)^3 - R_s^3).$$

This quantity is the global average of s^2.

3.4. A Simple Model: Uniform Heating

In this case, we assume a limit where there is no heating profile around the ionization bubble. We should get back the result derived in Section 3.1.1.

If there are no heating shells, the second term of Equation (33) and second and third terms of Equation (38) can be dropped. In this limit, we also obtain $R_h = R_x$, $E(r, R_x, R_x) = D(r, R_x)$, and $f_b = f_n$.

Simplifying the results of Sections 3.3.1–3.3.3,

$$\begin{aligned}
\langle n_1 n_2 \rangle &= f_n - f_n \sum_{R_x} N(R_x) \frac{4\pi}{3} R_x^3 D(r, R_x) \\
\langle n_1 s_2 \rangle &= s_b f_n - s_b f_n \sum_{R_x} N(R_x) \frac{4\pi}{3} R_x^3 D(r, R_x) \\
\langle s_1 s_2 \rangle &= s_b^2 f_n - s_b^2 f_n \sum_{R_x} N(R_x) \frac{4\pi}{3} R_x^3 D(r, R_x) \\
\langle n_1 s_1 \rangle &= s_b f_b = s_b f_n.
\end{aligned}$$

The total correlation is given by

$$\begin{aligned}
\mu &= (1 + \xi)(\langle n_1 n_2 \rangle - 2\langle n_1 s_2 \rangle + \langle s_1 s_2 \rangle) - (f_n - \langle n_1 s_1 \rangle)^2 \\
&= (1 + \xi)(1 - 2 s_b + s_b^2) f_n \left(1 - \sum_{R_x} N(R_x) \frac{4\pi}{3} R_x^3 D(r, R_x) \right) \\
&\quad - (f_n - s_b f_n)^2 \\
&= (1 - s_b)^2 ((1 + \xi) \langle n_1 n_2 \rangle - f_n^2).
\end{aligned}$$

This expression agrees with Equation (26) from Section 3.1.1. Our model goes to the correct limit for this simplified case.

Here, if we take only one bubble size, we have

$$\mu = (1 - s_b)^2 f_n ((1 + \xi)(1 - (1 - f_n) D(r, R_x)) - f_n). \qquad (45)$$

3.5. A Simple Model: One Bubble Size, Flat Heating Profile

One of the principal aims of this paper is to establish the new scales that emerge in the H I correlation function for a partially heated universe. For a fully heated universe ($T_S \gg T_{\mathrm{CMB}}$ in neutral regions), these scales are determined by the size distribution of ionized regions. In the partially heated case, there is a separation between unheated and heated neutral regions. This situation is expected to introduce new scales linked to the sizes of heated regions. Our detailed analysis of the physical conditions that exist during the early phase of reionization is difficult to interpret in terms of demarcated ionized, heated, and unheated regions, because unlike ionized regions, which have sharp boundaries, the heated regions have shallow profiles that smoothly merge into the background. However, for the purposes of understanding our formalism, we consider a simple model: a single bubble size (both ionized and heating) and a heating profile with a uniform temperature (flat). Thus, there are small ionization bubbles embedded in larger heated bubbles. We first ignore density fluctuations for simplicity in this section and later present the results including these perturbations. In this case, there are only three values of $\psi = n(1 - s)$ present in the universe: ψ_i, ψ_h, and ψ_b. Here $\psi_i = 0$, since $n = 0$ inside the ionized region. In the heated and background regions, respectively,

$$\begin{aligned}
\psi_h &= (1 - s_h) = 1 - \frac{T_{\mathrm{CMB}}}{T_{\mathrm{heat}}} \\
\psi_b &= (1 - s_{\mathrm{bg}}) = 1 - \frac{T_{\mathrm{CMB}}}{T_{\mathrm{bg}}}.
\end{aligned}$$

If N is the number density of the bubbles, then the total ionized volume fraction of the universe and the heated volume fraction

without correcting for overlap are, respectively,

$$f_i = \frac{4\pi}{3} R_x^3 N f_{hb} = \frac{4\pi}{3}(R_h^3 - R_x^3)N,$$

where R_x is the ionization bubble radius and R_h is the heating bubble radius. Allowing for overlap, the actual heated volume fraction and the remaining nonheated volume fraction are, respectively,

$$f_h = \frac{f_{hb}(1 - f_i)}{1 + f_{hb}} f_b = 1 - f_i - f_h,$$

This allows us to calculate the dimensionless temperature correlation:

$$\begin{aligned}\mu &= \langle \psi_1 \psi_2 \rangle - \langle \psi \rangle^2 \\ &= \psi_h^2 P((\psi_1 = \psi_h) \cap (\psi_2 = \psi_h)) \\ &\quad + 2\psi_h \psi_b P((\psi_1 = \psi_h) \cap (\psi_2 = \psi_b)) \\ &\quad + \psi_b^2 P((\psi_1 = \psi_b) \cap (\psi_2 = \psi_b)) - \langle \psi \rangle^2.\end{aligned}$$

Now we derive each term separately,

$$\begin{aligned}&P((\psi_1 = \psi_h) \cap (\psi_2 = \psi_b)) \\ &\quad = P(\psi_1 = \psi_h) P((\psi_2 = \psi_b) | (\psi_1 = \psi_h)) \\ &\quad = f_h f_b C(r, R_x, R_h, R_h). \end{aligned} \tag{46}$$

The other terms give

$$\begin{aligned}&P((\psi_1 = \psi_h) \cap (\psi_2 = \psi_h)) \\ &\quad = P(\psi_1 = \psi_h) - P((\psi_2 \neq \psi_h) \cap (\psi_1 = \psi_h)) \\ &\quad = f_h - P((\psi_2 = \psi_b) \cap (\psi_1 = \psi_h)) \\ &\qquad - P((\psi_2 = \psi_i) \cap (\psi_1 = \psi_h)) \\ &\quad = f_h - f_h f_b C(r, R_x, R_h, R_h) - f_i f_h C(r, 0, R_x, R_h) \\ &\qquad - f_i(1 - f_i)(C(r, 0, R_x, R_x) - C(r, 0, R_x, R_h)). \end{aligned} \tag{47}$$

In Equation (47), the third and fourth terms represent the correlation of the ionized and heated regions of different bubbles and the same bubble, respectively:

$$\begin{aligned}&P((\psi_1 \\ &\quad = \psi_b) \cap (\psi_2 = \psi_b)) = P(\psi_1 = \psi_b) \\ &\qquad - P((\psi_1 = \psi_b) \cap (\psi_2 = \psi_h)) \\ &\qquad - P((\psi_1 = \psi_b) \cap (\psi_2 \psi_i)) \\ &\quad = f_b - f_b f_h C(r, R_x, R_h, R_h) - f_b f_i C(r, 0, R_x, R_h). \end{aligned} \tag{48}$$

Putting the terms in Equations (46), (47), and (48) together, we have

$$\begin{aligned}\mu = \psi_h^2 &(f_h - f_h f_b C(r, R_x, R_h, R_h) - f_i f_h C(r, 0, R_x, R_h) \\ &- f_i(1 - f_i)(C(r, 0, R_x, R_x) - C(r, 0, R_x, R_h))) \\ &+ 2\psi_h \psi_b f_h f_b C(r, R_x, R_h, R_h) \\ &+ \psi_b^2 f_b (1 - f_h C(r, R_x, R_h, R_h) - f_i C(r, 0, R_x, R_h)) \\ &- (f_h \psi_h + f_b \psi_b)^2. \end{aligned} \tag{49}$$

If the impact of the density perturbations is included, we get

$$\begin{aligned}\mu = (1 + \xi)[\psi_h^2 &(f_h - f_h f_b C(r, R_x, R_h, R_h) \\ &- f_i f_h C(r, 0, R_x, R_h) \\ &- f_i(1 - f_i)(C(r, 0, R_x, R_x) - C(r, 0, R_x, R_h))) \\ &+ 2\psi_h \psi_b f_h f_b C(r, R_x, R_h, R_h) \\ &+ \psi_b^2 f_b (1 - f_h C(r, R_x, R_h, R_h) - f_i C(r, 0, R_x, R_h))] \\ &- (\psi_b f_b + \psi_h f_h)^2. \end{aligned} \tag{50}$$

To verify the validity of our formalism, we need to consider Equations (49) and (50) in different limits. (a) At large scales, all the functions $C(.,.,.,.)$ tend to unity. In this case, Equation (49) vanishes, and Equation (50) approaches the correct large-scale limit (Equation (28)). (b) In the case of $\psi_b = \psi_h$, there is no distinction between the heated bubble and the background, and we expect the correlation information from the heated bubbles to disappear. In this case, Equation (50) reduces to Equation (45), the case in which only ionized bubbles and density perturbations contribute to the correlation. One subcase of this scenario is when both ψ_b and ψ_h approach unity, the limit in which the entire universe is uniformly heated at high temperatures $T_S \gg T_{\rm CMB}$. (c) Finally, if we assume $R_h \to R_x$, $f_h = 0$, and $f_b = f_n$, we get

$$\begin{aligned}\mu &= (1 + \xi)[\psi_b^2 f_b (1 - f_i C(r, 0, R_x, R_h))] - (\psi_b f_b)^2 \\ &= (1 + \xi)[(1 - s_b)^2 f_n (1 - (1 - f_n) C(r, 0, R_x, R_x))] \\ &\quad - ((1 - s_b) f_n)^2 \\ &= (1 - s_b)^2 f_n ((1 + \xi)(1 - (1 - f_n) D(r, R_x)) - f_n). \end{aligned}$$

This is the same result as Equation (45).

The agreement of our formulation with the expected results in different limits shows we have taken into account the relevant physical processes in our study.

Our formalism allows for negative correlation. Such a situation might arise if $s > 1$ inside the heated bubble and $s < 1$ in the background. However, we do not find many instances of negative correlation in all the cases we study here, even when we neglect density correlations. As ξ is positive for all the scales we consider in this paper, inclusion of this term ensures we do not get negative correlation in any case. We check that we can generate negative correlation by assuming the centers of ionizing bubbles to be anticorrelated.

4. Results

The brightness temperature correlation is caused by density, ionization, and heating inhomogeneities. The main aim of this paper is to study the era dominated by heating inhomogeneities. There are two main effects in modeling the correlations in this era. (a) The near-zone effect introduces new scales corresponding to heated bubbles around self-ionized bubbles (Figures 3 and 4). The correlation function during the partially heated era is determined by the scales of these bubbles, which are much larger than the ionization bubbles. (b) The evolution of $s = T_{\rm CMB}/T_K$ in the far zone starting from an era where s can exceed unity.

We explore four modeling parameters in this paper: photoionization efficiency ζ, X-ray spectral index α, number

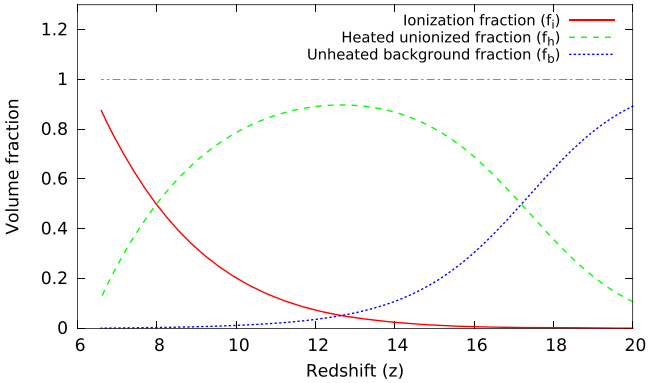

Figure 8. Evolution of ionized and heating fractions for a fiducial model (described in the text) for $\zeta = 10$, $N_{\rm heat} = 1$, and $\alpha = 1.5$.

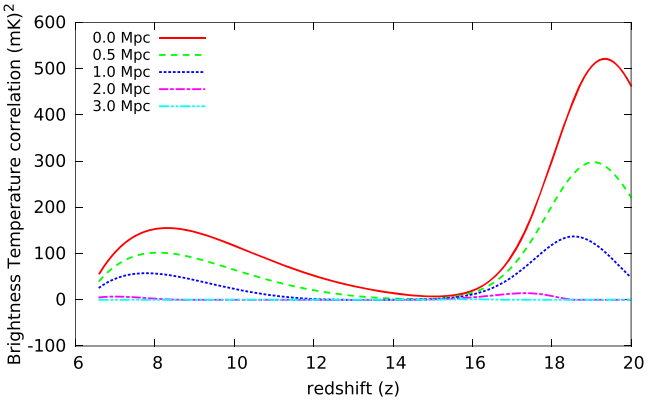

Figure 9. Evolution of the correlation function for a set of scales for the model in Figure 8.

of X-ray photons per stellar baryon $N_{\rm heat}$, and minimum X-ray frequency escaping the source halo $\nu_{\rm min}$. These parameters have already been introduced in Sections 2.1 and 2.2. Here ζ is constrained by Planck results that fix the optical depth to the reionization surface; ζ in the range 10–15 is in agreement with these results (Figure 1; Planck Collaboration et al. 2016). We take runs in the redshift range 10–20.

4.1. Simple Model

To understand the evolution of the correlation function at a given scale, we first consider the simple model based on an initial bubble distribution given by an ionized bubble of a single size that is surrounded by a heating bubble of a single profile temperature (flat heating profile), with the ratio of heating to ionized bubble size remaining constant (Section 3.5). We also neglect the impact of density perturbations in this case. We show the evolution of the ionized, heated, and background fractions—f_i, f_h, and f_b—for such a case in Figure 8. The initial radius of the ionized (heated) bubble is assumed to be 0.1 Mpc (0.7 Mpc). The initial ratio of the heated and ionized fractions is the cube of the ratio of these radii. Initially, nearly 90% of the universe is in the phase outside the heated bubbles. As the universe evolves, the ionized bubbles grow, and so do the heated bubbles, resulting in an increase in both the ionized and heated fractions with a decrement of the background fraction. This process is accompanied with an increase in the background and bubble temperatures. At a certain redshift, the heated bubble begins to merge, driving the background fraction to zero. Eventually, the ionized fraction becomes large enough to drive the heated fraction to zero.

The evolution of the correlation function (normalized using Equation (2)) for a set of scales is shown in Figure 9.[5] Here the background temperature is assumed to evolve according to Equation (17) for the modeling parameters $\zeta = 10$, $N_{\rm heat} = 1.0$, and $\alpha = 1.5$, while the heating bubble temperature is kept at a constant value above the background temperature. Initially, the correlation function is small, which is expected, because the function tends to zero as f_i and f_h approach zero in the absence of density perturbations. The correlation function rises as f_h increases and then decreases again owing to multiple reasons.

There are three distinct factors that can wipe out the information on the correlation scales generated by heating inhomogeneities. (a) An increase in temperature in the heated bubbles and the background. When these temperatures rise substantially above $T_{\rm CMB}$, $s = T_{\rm CMB}/T_S$ is driven to zero, causing both the autocorrelation of s and its cross-correlation with the ionization inhomogeneities to approach zero. This is the primary cause of the evolution of the correlation function, as seen in Figure 9. (b) A decrease in the gradient of the temperature between the heated bubble and the background. This effect plays an important role when the fuzzy boundaries of the heating regions are taken into account, which we discuss in the next section. It can also be achieved when $\nu_{\rm min}$ is increased, as seen in Figure 3. In this case, the heating inside the bubble decreases, and most of the X-ray photons are used in raising the background temperature. We discuss this case in the next section. (c) Merging of bubbles. This process destroys the distinction between the heated bubble and the background, thereby erasing the correlation information on the scales of the bubbles. The difference between this case and case (b) is that the latter is possible for even small heating fractions, f_h.

All these reasons play some role in determining the transition from heating to the ionization inhomogeneities regime. For the parameters we consider in this paper, the effect of both cases (a) and (c) can be suppressed by considering a small $N_{\rm heat}$, while the scenario considered in case (b) can be achieved by varying $\nu_{\rm min}$.

This behavior is generic to all models, even though the evolution on the range of scales displayed in Figure 9 could change as it is determined by the sizes of the heating bubbles. For instance, in Figure 9, the correlation on the scales of $\simeq$3 Mpc remains close to zero at all times owing to our choices of initial scales. The magnitude of the correlation function is also determined by the background and heated temperatures. Both rise as the universe evolves, decreasing s and therefore decreasing the correlation function. In Figure 9, $T_h^{-1} f_h + T_b^{-1} f_b$ reaches $T_{\rm CMB}^{-1}$ at $z \simeq 16$; at this redshift, the global H I signal vanishes, and the universe makes a transition from being observable in the H I signal from absorption to emission. However, as discussed above, the redshift at which the correlation function reaches its minimum is determined by a multitude of other causes, and this transition is reached at $z \simeq 15$.

[5] We also show the evolution of the rms, which corresponds to the plot for $r = 0$, to guide the eye. For an experiment, the relevant quantity would be the rms smoothed with the three-dimensional resolution of the radio interferometer, which, as discussed below, could be around 3–5 Mpc for ongoing and upcoming experiments. Therefore, the measured rms would always be smaller than the quantity shown in Figure 9.

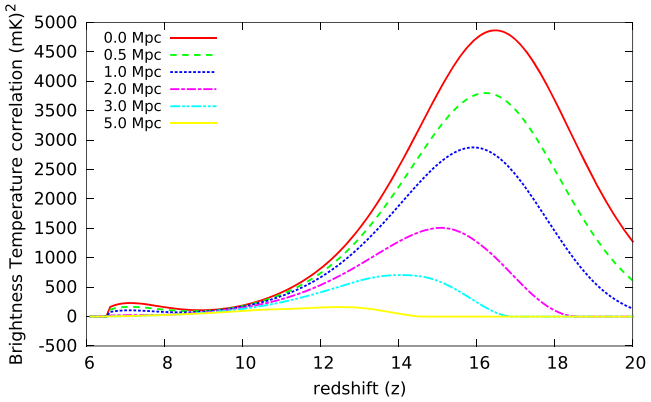

Figure 10. Evolution of the correlation function for a set of scales for a model in which the background temperature is held constant (see text for details).

The minimum of the correlation function around $z \simeq 15$ signals the beginning of the phase in which the universe is uniformly heated. The signal at this time reaches nearly zero for all scales in our case, because $f_i \simeq 0.01$ at the time of the heating transition; therefore, the ionization inhomogeneities are small, and we ignore the density perturbations. As the ionized fraction increases, the ionization inhomogeneities start rising, reaching a peak around $f_i \simeq 0.5$, and subsequently decline as the universe becomes fully ionized. It should be noted that the peak of the correlation function when it is dominated by ionization inhomogeneities is smaller than when it is determined by heating inhomogeneities. This is expected, as s is larger than unity in the earlier phase and zero during the later phase.

To isolate the impact of merging from the effect of heating on the evolution of the correlation function, we show in Figure 10 a different model, which is also based on the evolution of the ionization and heating fractions shown Figure 8. In this case, the initial background temperature is 5 K, the temperature inside the heated bubble is 10 K, and the temperatures are kept at their initial values throughout. Therefore, in this case, the heating inhomogeneities are destroyed by the merging of the heating bubbles and not the heating, which delays the transition to the uniform heating regime as compared to Figure 9.

Figures 9 and 10 allow us to identify the relevant physical processes involved in the modeling of the correlation function in the phase when heating inhomogeneities dominate, the end of this phase (owing to either heating above CMB temperature or merger), and the transition to ionization inhomogeneities domination phase. As we shall notice later, the features seen in the figures are also present when more exact modeling is attempted. In this paper, we assume the centers of ionization bubbles to be uncorrelated. If the centers are correlated, new correlation scales can emerge; we briefly discuss this scenario in Appendix C.

4.2. Complete Model

In this subsection, we present results for the complete model based on the ΛCDM model. This generalizes the case discussed in the previous subsection in the following aspects: (a) there is a size distribution of the ionization and heating bubbles (Figures 2 and 5), and (b) the heating bubbles have shallow profiles (Figure 4), which makes it harder to identify the impact of the sizes of the heating bubbles on the correlation function.

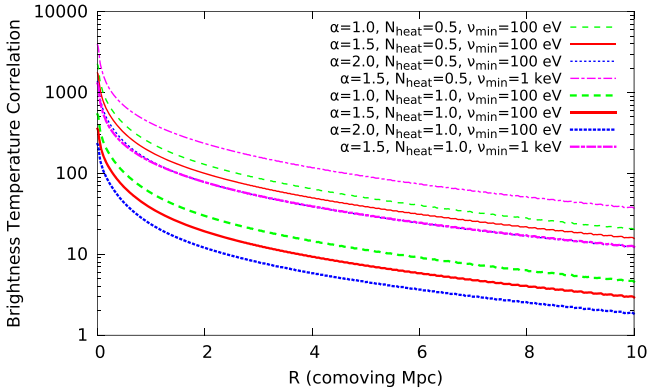

Figure 11. Two-point correlation functions for different values of $N_{\rm heat}$, α, and $\nu_{\rm min}$ for $\zeta = 10$ at $z = 17$.

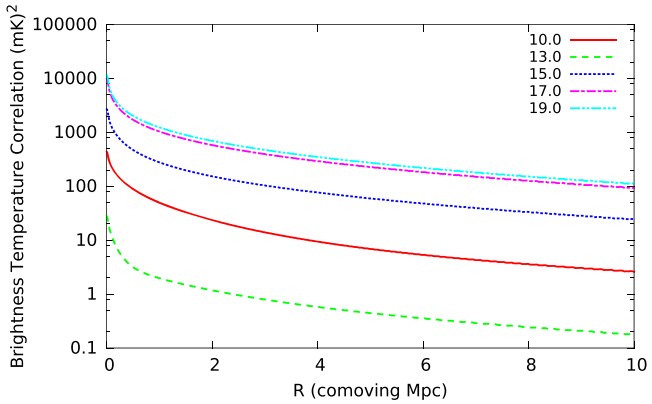

Figure 12. Evolution of the correlation function for $\alpha = 1.5$, $\zeta = 10$, and $N_{\rm heat} = 0.1$.

Dependence on modeling parameters and redshift. In Figure 11, we show the correlation functions for the complete model for different choices of modeling parameters using Equations (2), (6), (16), (17), (25), (32), (36), and (44). The correlation functions shown in the figure are large at small scales (Equation (29)), decrease as the distance between two points increases, and approach Equation (28) at large scales. On intermediate scales, the structure of the correlation function is determined by the size distribution of the heated bubbles (e.g., Figure 5).

As the value of the spectral index α is increased for a fixed $N_{\rm heat}$, there are more low-frequency photons resulting in a higher background temperature (Figure 3); this results in a decrease in the correlation function as it scales as $(1 - s_b) = (1 - \langle s \rangle)$ during this phase (Equation (28)). For the same reason, when $N_{\rm heat}$ is increased, the correlation decreases. Figures 12 and 13 show the correlation function at different redshifts for different values of $N_{\rm heat}$. At high redshifts, the correlation function is large owing to a smaller background temperature. As the universe gets heated, s_b decreases, reaching f_n at a certain redshift and resulting in the vanishing of the correlation function at large scales (Equation (28)). As the s_b decreases further, the impact of partial heating disappears, the correlation function increases again owing to ionization inhomogeneities, and the H I signal is now observable in emission. We have already seen this transition for the single-bubble, flat heating profile case (Figures 9 and 10). In Figure 14, we show the evolution of the global H I signal for a range of parameters. The dependence

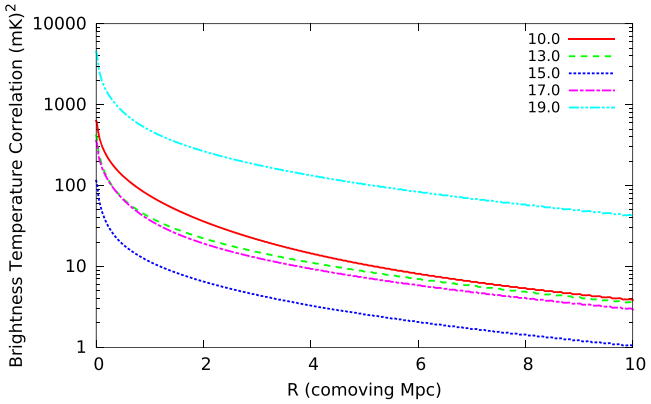

Figure 13. Evolution of the correlation function for $\alpha = 1.5$, $\zeta = 10$, and $N_{\rm heat} = 1$.

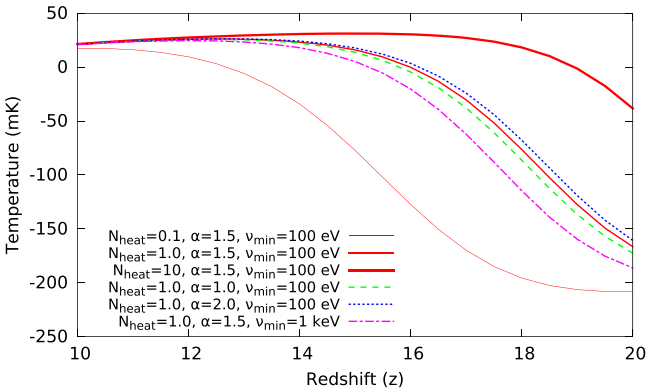

Figure 14. Evolution of the global brightness temperature $\langle \Delta T_b \rangle$ (Equation (2)) for a range of parameters for $\zeta = 10$.

of the strength and the transition from absorption to emission of the signal on different parameters is as expected from the discussion in this section.

We show the evolution of the correlation function for a range of scales in Figure 15 for different values of $N_{\rm heat}$ and $\nu_{\rm min}$. For a smaller value of $N_{\rm heat}$ and larger value of $\nu_{\rm min}$, the heating transition is delayed, and the signal is larger during the era of partial heating, in line with the discussion in the foregoing; this result is in qualitative agreement with similar analyses of delayed heating, e.g., Fialkov et al. (2014).

Correlation scales. The scales at which we expect significant correlation are determined by the distribution of the sizes of the heating bubbles, whose sizes are determined by the sizes of the ionization bubbles, R_x, the heating parameter $N_{\rm heat}$, α, and $\nu_{\rm min}$ (Equation (16)). In Figure 5, we show the size distribution of the heating bubbles for a set of parameters. The heating bubbles are larger than the self-ionized bubbles by roughly a factor of 4.5 for this case and at $z \simeq 14$, and the heating scales lie in the range 2–7 Mpc. However, as noted above, the correlation function depends on the gradient of the temperature, and the fuzziness of the heating bubble does not allow one to readily identify these scales in the correlation function.

Generically, a larger $N_{\rm heat}$ for a fixed R_x results in larger heating bubbles and therefore causes correlation at larger scales. An increase in $\nu_{\rm min}$ causes shallow heating profiles, which results in reducing the gradient of the temperature between the heating bubbles and the background, thereby reducing the correlation on a given scale for the same background temperature.

In this paper, we consider a set of models in which parameters such as $N_{\rm heat}$ and $\nu_{\rm min}$ do not evolve with time. If these parameters are allowed to evolve, the relation between the temperature inside the heating bubbles and the background temperature would be more complicated. For instance, if R_x is larger at an earlier epoch owing to the evolution of ζ, the heating bubbles could be larger, causing correlations on much larger scales than shown in this paper.

Can the merger of heating bubbles introduce new correlation scales? In this paper, we assume the centers of ionization bubbles to be uncorrelated. It should be noted that the positions of the ionizing sources are expected to be highly correlated, and this effect has already been included in the definition of self-ionized bubbles. However, the mean bubble separation corresponds to much larger scales at which the density correlation function for the ΛCDM model is much smaller than unity, and on such scales, the H I correlation function of the density field is expected to be smaller. The correlation of different ionizing centers is expected to follow the correlation function of the density field with a bias (e.g., Dodelson 2003 and references therein). In this case, the merging process is nearly homogeneous and therefore does not introduce any new scales; its main effect, as noted above, is to wipe out the correlation scales of the heated bubbles. It also follows that if the centers of the self-ionized bubbles are assumed to be correlated, then, in principle, correlation at much larger scales can emerge. This can occur if the H I field is highly biased with respect to the underlying density field (Ahn et al. 2015b). We consider the case of correlated ionizing centers in Appendix C and show that, while this effect does not alter our results qualitatively, it can introduce correlations at new scales.

Power spectrum, comparison with existing results, and the topology of early reionization. The early phase of reionization has been extensively studied in the literature using semi-analytic methods but primarily large-scale simulations (e.g., Pritchard & Furlanetto 2007; Visbal et al. 2012; Mesinger et al. 2013; Tashiro & Sugiyama 2013; Fialkov et al. 2014, 2015, 2017; Pacucci et al. 2014; Ghara et al. 2015). Most of these studies have been in the Fourier space. Our analysis suggests that real-space correlation allows us to identify the physical processes more readily. Our results show that the entire correlation structure in real space can be written in terms of a single function, $C(.,.,.,.)$, and its limits given by the functions $E(.,.,.)$ and $D(.,.)$ (Appendix B). A Fourier transform with respect the first argument r of this function yields the power spectrum. In Figure 16, we show the evolution of the power spectrum for a range of Fourier modes k for different values of $N_{\rm heat}$ and $\nu_{\rm min}$ (for details, see Appendix B6).

Existing results show that for $k \simeq 0.1$–$0.5\,{\rm Mpc}^{-1}$,[6] during the era of early reionization where heating inhomogeneities dominate, there is a peak in the power spectrum that is followed by a smaller peak at lower redshifts when the inhomogeneities are dominated by ionization inhomogeneities (e.g., Pritchard & Furlanetto 2007; Fialkov et al. 2014; Ghara et al. 2015). Our results (Figure 16) are in agreement with this general picture.

[6] Generally, a wavenumber k will contribute to a range of spatial scales; for making a comparison between a real-space correlation function and a power spectrum, one can use the approximate conversion $r \simeq \pi/k$.

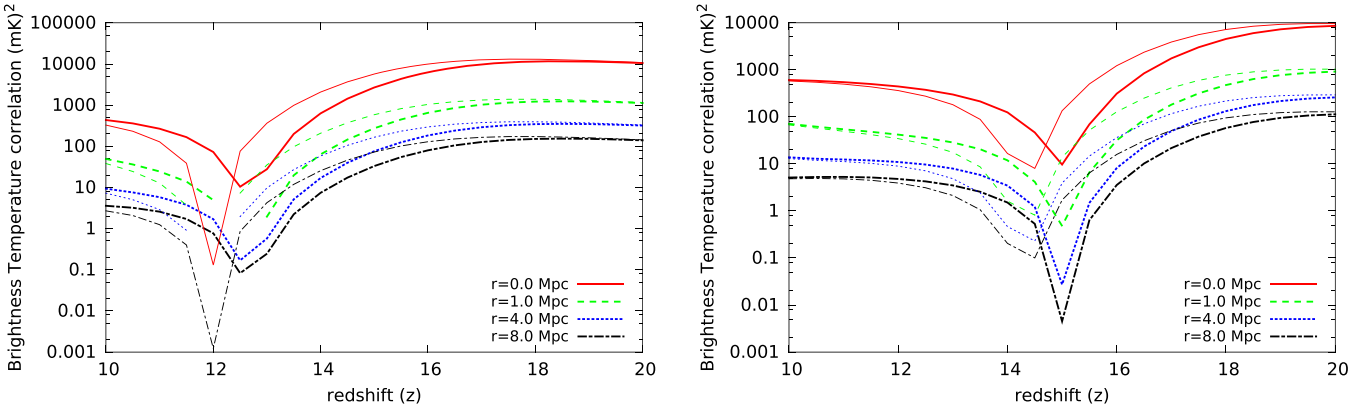

Figure 15. Evolution of the two-point correlation function for a range of scales (including the rms corresponding to $r = 0$) for $\alpha = 1.5$, $\zeta = 10$, and two values of $\nu_{\rm min}$. The thick curves are for $\nu_{\rm min} = 100$ eV, and the thin curves are for $\nu_{\rm min} = 1$ keV. The left and right panels correspond to $N_{\rm heat} = 0.1$ and 0.5, respectively.

They are also in agreement with analyses that have studied the impact of partial-heating density perturbations at large scales (e.g., Mesinger et al. 2013; Tashiro & Sugiyama 2013)[7] or the impact of late heating on the fluctuating component of the signal (Fialkov et al. 2014). Many of these analyses strongly suggest that the H I signal is a robust probe of early X-ray heating, an inference our analysis adequately captures. We also establish the dependence of the signal on different parameters, which agrees with the existing results. We do not attempt a more detailed comparison with the existing results because it is hard to establish a one-to-one relation between the parameters we use and those in the literature.

Our results are based on the assumption that the topology of the early reionization is given by Figure 6: an ionized sphere surrounded by a fuzzy heated region that merges smoothly into the background. The density perturbations determine the size of the ionized regions, but the brightness temperature correlations on the scales of heating bubbles are dominated by heating autocorrelation and heating-ionization cross-correlation.

The assumption of the sphericity of the ionized and heating regions for the computation of the correlation function is reasonable even in the presence of density perturbations because the reionization process is statistically isotropic and homogeneous.[8] However, the inclusion of density cross-correlation with other fields can alter the correspondence between the scales for a given set of physical parameters; e.g., the scale of the heating bubble is given roughly by the distance at which the optical depth of an X-ray photon reaches unity. We retain only the background density for this computation, but to be more exact, we need to also include the impact of the density perturbations at this scale. Generally, the correlation of the H I density field is small unless the H I field is highly biased with respect to the underlying density field, so this correction should be small at high redshifts but will become more important at smaller redshifts. Also, we assume that the ionizing centers are uncorrelated; this assumption has greater validity at higher redshifts, when the mean separation between the centers is larger. At smaller redshifts ($z \lesssim 12$, depending on the parameter ζ), the excursion set formalism begins to break down, since the ionization fraction becomes large and there is substantial overlap between ionization bubbles. In this regime, our results are not very accurate; however, we still show results up to $z \simeq 10$, to emphasize the transition from the era of domination of heating inhomogeneities to ionization inhomogeneities.

While *N*-body simulations assume paramount importance if the H I density field at large redshifts is to be directly imaged, all of the ongoing experiments that seek to detect this signal rely upon statistical detection of this signal. Our method cannot predict the shape of individual regions but allows us to compute the statistics of the H I field. Another advantage with analytic estimates is that they are computationally inexpensive as compared to simulations. Given the uncertainty in the early-heating phase of the universe, our analysis can be used to compare the observed signals for multiple sets of parameters and better understand their degeneracies at a fraction of the computational cost needed to carry out an *N*-body simulation. For instance, the H I signal in the early-heating regime depends on the gradient of the temperature in and across heated regions whose sizes depend on multiple physical processes. It would be of great interest to determine whether future data can distinguish between these different physical processes.

Detectability of the signal. Many operational (e.g., LOFAR, MWA, PAPER, GMRT) and upcoming (HERA, SKA) radio interferometers have the capability to detect the fluctuating component of the H I signal in the redshift range $8 < z < 25$ (for details, see, e.g., Mesinger et al. 2014; Ahn et al. 2015a; Koopmans et al. 2015). It is customary in the literature to present the sensitivity of radio interferometers for the detection of the H I signal in terms of power spectrum, partly because the radio interferometers measure the Fourier component of the H I signal. However, these estimates can be extended to the image plane (which is often a by-product of the analysis pipeline; e.g., Patil et al. 2017 for LOFAR) or the real-space correlation functions used for computation of the signal in this paper (e.g., Sethi & Haiman 2008). We discuss here the expected

[7] At large scales, the correlation function approaches Equation (28), which is determined by density inhomogeneities; its value could be enhanced by $(1 - \langle s \rangle)^2$ at early times. Therefore, a large-scale correlation function at early times could be a reliable measure of density correlation and its statistical anisotropy, in agreement with the results of Mesinger et al. (2013) and Tashiro & Sugiyama (2013).

[8] We neglect redshift space distortion in the paper, which renders the density field statistically anisotropic. However, so long as the ionization and heating sources are isotropic, their correlation is not affected by this anisotropy.

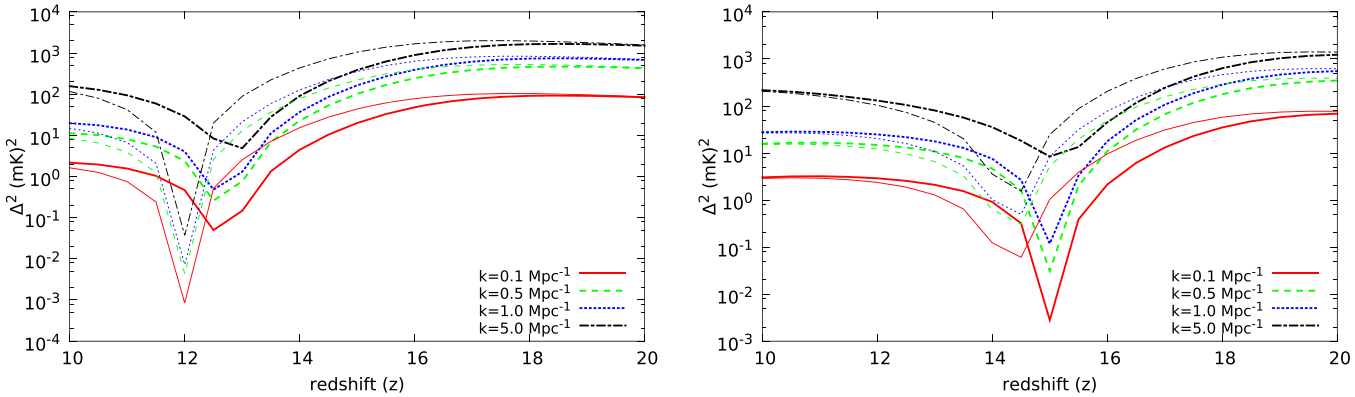

Figure 16. Evolution of $\Delta^2 = k^3P(k)/2\pi^2$ $((mK)^2)$ for a range of scales for $\alpha = 1.5$, $\zeta = 10$, and two values of $\nu_{\rm min}$. The thick curves are for $\nu_{\rm min} = 100$ eV, and the thin curves are for $\nu_{\rm min} = 1$ keV. The left and right panels correspond to $N_{\rm heat} = 0.1$ and 0.5, respectively.

sensitivity of SKA1-LOW (Koopmans et al. 2015). For a deep survey with SKA1-LOW, the error on the power spectrum ($\Delta^2 \equiv k^3P(k)/(2\pi^2)$) is expected to vary from $0.1\,({\rm mK})^2$ at $z \simeq 9$ to $5\,({\rm mK})^2$ at $z \simeq 25$ for $k = 0.1\,{\rm Mpc}^{-1}$. At $z \simeq 16$, the expected error is $2\,({\rm mK})^2$, increasing to $10\,({\rm mK})^2$ for $k \simeq 0.5\,{\rm Mpc}^{-1}$ (for details, see Figure 2 of Koopmans et al. 2015). Direct comparison with Figure 16 shows that the H I signal at $z \simeq 16$ can be detected with a signal-to-noise ratio varying from 50 to 10 for $0.1\ {\rm Mpc}^{-1} < k < 0.5\,{\rm Mpc}^{-1}$.

We can get similar estimates from the signal in real space by using $r \simeq \pi/k$.[9]

5. Summary and Conclusions

The main aim of this paper is to present a new analytic formalism to study the phase of the EoR that is dominated by partial heating.

The main ingredients of our analytic model are as follows. (a) The correlation of the H I density field is given by the ΛCDM model. At large scales, this correlation dominates (Equation (28)). (b) The correlation of the ionization is determined by the size distribution of the self-ionized bubbles. The definition of self-ionized bubbles takes into account the clustering of halos as they form in high-density regions. The cross-correlation between density and ionization inhomogeneities is neglected in our work. Cases (a) and (b) have been extensively studied both analytically and numerically in the literature. (c) The modeling of heating inhomogeneities uses the near and far zones around the centers of the self-ionized regions. While the phase of partial heating has been studied in the literature, this formulation is new and allows us to compute the statistical quantities related to the H I signal. (d) Two-point correlation functions are computed in real space for a sharp ionized region surrounded by a fuzzy heated bubble. We develop a formalism to compute these functions. In particular, we take into account the heating autocorrelation and heating-ionization cross-correlations while neglecting the density-heating cross-correlation. We also take into consideration the correlation for both a single bubble and multiple bubbles, assuming the centers of self-ionized regions to be uncorrelated. We also explicitly show that our formalism reduces to the correct form in different limits (discussion following Equation (50)). In many extensions of the ΛCDM model, the power at small scales can differ substantially from the usual model (e.g., Sethi & Subramanian 2009; Sarkar et al. 2016); our formalism can be extended to such models by generating the size distribution of the self-ionized bubbles using the matter power spectra of these models.

We model the ionization and heating using four parameters: ζ, which determines the ionization history of the EoR and is constrained by the *Planck* and *WMAP* results, and three parameters to model heating—$N_{\rm heat}$, the number of X-ray photons per stellar baryon; α, the spectral index of the X-ray photons; and $\nu_{\rm min}$, the lowest frequency of the X-ray photons. We study the impact of these parameters on the correlation functions and find reasonable agreement with existing results.

In this paper, we assume a homogeneous coupling between Lyα photons and neutral hydrogen through the Wouthuysen–Field effect such that $T_\alpha = T_K$. As discussed in Section 2.3, this is a good assumption for $z < 20$, but we expect imperfect coupling at higher redshifts that could create inhomogeneities in the H I signal, resulting in another peak in the evolution of the signal at multiple scales (e.g., Pritchard & Furlanetto 2007; Chen & Miralda-Escudé 2008; Ahn et al. 2015a). These inhomogeneities arise owing to the absorption of photons between Lyβ and the Lyman limit closer to the ionizing sources, unlike the photons between Lyα and Lyβ discussed in Section 2.3, and these inhomogeneities can be studied using the formalism developed in this paper. We hope to return to this issue in the near future.

Given the uncertainty in the heating history during the EoR and its impact on the H I signal, our analytic formulation allows us to isolate the impact of different physical parameters and underline their degeneracies. Future data in the redshift range of interest, $10 < z < 20$, are likely to put strong constraints on the physical processes during this era. Our work is one step in the direction of understanding the data better.

[9] The angular scale above which the H I signal can be reliably measured for most ongoing and upcoming radio interferometers is a few arcminutes; $1'$ corresponds to nearly 3 Mpc (comoving) at $z \simeq 15$, or these telescopes are sensitive to linear scales larger than 5–10 Mpc (comoving). However, these telescopes have frequency resolutions that correspond to much smaller linear scales; e.g., MWA's frequency resolution of 40 kHZ corresponds to nearly 1 Mpc (comoving) along the line of sight. The 3D H I signal is probed with a different resolution on the sky plane as compared to the line of sight.

We would like to thank Saurabh Singh, Steven Furlanetto, and Jordan Mirocha for useful discussions and comments on the manuscript.

Appendix A
Probability

Here

$$P(A|B) = \frac{P(A \cap B)}{P(B)}, \tag{51}$$

$$P((A \bigcap B)|C) = P(A|(B \bigcap C))\, P(B|C), \tag{52}$$

$$P(A \bigcap B) = P(A) - P(A \bigcap \tilde{B}). \tag{53}$$

Appendix B
Geometry

B.1. A(R_1, R_2, d)

Given two spheres of radius R_1 and R_2, the surface area of the sphere of radius R_1 that lies inside the sphere of radius R_2 is[10]

$$A(R_1, R_2, d) = \begin{cases} 0 & d > R_1 + R_2 \\ 0 & d < R_1 - R_2 \\ 4\pi R_1^2 & d < R_2 - R_1, \\ \frac{\pi R_1 (R_2 - R_1 + d)(R_2 + R_1 - d)}{d} & \text{Otherwise} \end{cases} \tag{54}$$

where $d =$ the distance between the two sphere centers.

B.2. V(R_1, R_2, d)

Given two spheres of radius R_1 and R_2, the overlapped volume is

$$V(R_1, R_2, d) = \begin{cases} 0 & d > R_1 + R_2 \\ \frac{4\pi}{3} R_2^2 & d < R_1 - R_2 \\ \frac{4\pi}{3} R_1^2 & d < R_2 - R_1 \\ \frac{\pi (R_2 + R_1 - d)^2 (d^2 + 2d(R_1 + R_2) - 3(R_1 - R_2)^2)}{12d} & \text{Otherwise} \end{cases},$$

where $d =$ the distance between the two sphere centers.

B.3. C(x, P, Q, R)

If point 1 is located between a distance P and Q ($P < Q$) from the center of a sphere, then $C(x, P, Q, R)$ is the probability that its neighbor point 2 at a distance x from point 1 is located outside the concentric sphere of radius R. We assume $a =$ the distance of point 1 from the center of the sphere.

(a) $x \leqslant R - Q$. None of the neighbors of point 1 are outside the sphere of radius R, giving $C(x, P, Q, R) = 0$.

(b) $x \leqslant P - R$. All of the neighbors of point 1 are outside the sphere of radius R, giving $C(x, P, Q, R) = 1$.

(c) $x \geqslant R + Q$. All of the neighbors of point 1 are outside the sphere of radius R, giving $C(x, P, Q, R) = 1$.

(d) $R - Q \leqslant x \leqslant R - P$. Taking $S = R - x$, we can see that all of the neighbors of the points between a distance P and S are inside the sphere of radius R. Therefore, we have

$$C(x, P, Q, R) = \left[\frac{\frac{4\pi}{3}(S^3 - P^3)}{\frac{4\pi}{3}(Q^3 - P^3)}\right](0) + \int_S^Q \left(1 - \frac{A(x, R, a)}{A_x}\right) \frac{4\pi a^2}{\frac{4\pi}{3}(Q^3 - P^3)} da,$$

where $A_x = 4\pi x^2$ is the area of a sphere of radius x.

(d.a) If $x \leqslant Q - R$, taking $T = x + R$, we see that all of the neighbors of the points between a distance T and Q are outside the sphere of radius R:

$$\begin{aligned} C(x, P, Q, R) &= \int_S^T \left(1 - \frac{A(x, R, a)}{A_x}\right) \frac{4\pi a^2}{\frac{4\pi}{3}(Q^3 - P^3)} da \\ &\quad + \int_T^Q \left(1 - \frac{0}{A_x}\right) \frac{4\pi a^2}{\frac{4\pi}{3}(Q^3 - P^3)} da \\ &= \frac{Q^3 - R^3}{Q^3 - P^3}. \end{aligned}$$

(d.b) Otherwise,

$$C(x, P, Q, R) = \frac{1}{2}\frac{Q^3 - (R - x)^3}{Q^3 - P^3} + \frac{3}{8x}\frac{Q^2 - (R - x)^2}{Q^3 - P^3} \times \left[\frac{Q^2 + (R - x)^2}{2} + (x^2 - R^2)\right].$$

(e) $P - R \leqslant x \leqslant Q - R$. Taking $S = R + x$, we can see that all the neighbors of the points between distance S and Q are outside the sphere of radius R. Therefore we have,

$$C(x, P, Q, R) = \left[\frac{\frac{4\pi}{3}(Q^3 - S^3)}{\frac{4\pi}{3}(Q^3 - P^3)}\right](1) + \int_P^S \left(1 - \frac{A(x, R, a)}{A_x}\right) \frac{4\pi a^2}{\frac{4\pi}{3}(Q^3 - P^3)} da.$$

(e.a) If $x \geqslant P + R$, $T = x - R$, and we can see that all of the neighbors of the points between a distance P and Q are

[10] mathworld.wolfram.com/Sphere-SphereIntersection.html; http://mathworld.wolfram.com/Zone.html

outside the sphere of radius R. Therefore, we have

$$C(x, P, Q, R) = \left[\frac{\frac{4\pi}{3}(Q^3 - S^3)}{\frac{4\pi}{3}(Q^3 - P^3)}\right](1) + \int_P^T \left(1 - \frac{0}{A_x}\right)\frac{4\pi a^2}{\frac{4\pi}{3}(Q^3 - P^3)}da + \int_T^S \left(1 - \frac{A(x, R, a)}{A_x}\right)\frac{4\pi a^2}{\frac{4\pi}{3}(Q^3 - P^3)}da = 1 - \frac{R^3}{Q^3 - P^3}.$$

(e.b) For $x \leqslant P + R$, there are two probabilities. If $x < R - P$, we are left with the case (d.b). Otherwise,

$$C(x, P, Q, R) = \frac{Q^3 - (R + x)^3/2 - P^3/2}{Q^3 - P^3} + \frac{3}{8x}\frac{(R + x)^2 - P^2}{Q^3 - P^3}\left[\frac{(R + x)^2 + P^2}{2} + (x^2 - R^2)\right].$$

(f) $R + P \leqslant x \leqslant R + Q$. Taking $S = x - R$, we can see that all of the neighbors of the points between a distance S and P are outside the sphere of radius R. Therefore, we have

$$C(x, P, Q, R) = \left[\frac{\frac{4\pi}{3}(S^3 - P^3)}{\frac{4\pi}{3}(Q^3 - P^3)}\right](1) + \int_S^Q \left(1 - \frac{A(x, R, a)}{A_x}\right)\frac{4\pi a^2}{\frac{4\pi}{3}(Q^3 - P^3)}da.$$

(f.a) If $x \leqslant Q - R$, $T = x + R$, and we can see that all of the neighbors of the points between a distance T and Q are outside the sphere of radius R. This is the same case as (e.a) (with T and S exchanged). Therefore, we have

$$C(x, P, Q, R) = 1 - \frac{R^3}{Q^3 - P^3}.$$

(f.b) Otherwise,

$$C(x, P, Q, R) = \frac{(x - R)^3 - P^3}{Q^3 - P^3} + \frac{1}{2}\frac{Q^3 - (x - R)^3}{Q^3 - P^3} + \frac{3}{8x}\frac{Q^2 - (x - R)^2}{Q^3 - P^3}\left[\frac{Q^2 + (x - R)^2}{2} + (x^2 - R^2)\right].$$

(g) For the last case, when $x \geqslant Q - R$, $x \geqslant R - P$, $x \leqslant P + R$,

$$C(x, P, Q, R) = \int_P^Q \left(1 - \frac{A(x, R, a)}{A_x}\right)\frac{4\pi a^2}{\frac{4\pi}{3}(Q^3 - P^3)}da = \frac{1}{2} + \frac{3}{8x}\frac{P + Q}{P^2 + PQ + Q^2} \times \left[\frac{P^2 + Q^2}{2} + (x^2 - R^2)\right],$$

$$C(x, P, Q, R) = \begin{cases} 0 & x \leqslant R - Q \\ 1 & x \leqslant P - R \\ 1 & x \geqslant R + Q \\ \frac{1}{2}\frac{Q^3 - (R - x)^3}{Q^3 - P^3} + \frac{3}{8x}\frac{Q^2 - (R - x)^2}{Q^3 - P^3}\left[\frac{Q^2 + (R - x)^2}{2} + (x^2 - R^2)\right] & R - Q \leqslant x \leqslant R - P,\ x > Q - R \\ \frac{Q^3 - R^3}{Q^3 - P^3} & R - Q \leqslant x \leqslant R - P,\ x \leqslant Q - R \\ \frac{1}{2}\frac{2Q^3 - (R + x)^3 - P^3}{Q^3 - P^3} + \frac{3}{8x}\frac{(R + x)^2 - P^2}{Q^3 - P^3}\left[\frac{(R + x)^2 + P^2}{2} + (x^2 - R^2)\right] & |P - R| \leqslant x \leqslant Q - R,\ x < P + R \\ 1 - \frac{R^3}{Q^3 - P^3} & P + R \leqslant x \leqslant Q - R, \\ \frac{1}{2}\frac{(x - R)^3 + Q^3 - 2P^3}{Q^3 - P^3} + \frac{3}{8x}\frac{Q^2 - (x - R)^2}{Q^3 - P^3}\left[\frac{Q^2 + (x - R)^2}{2} + (x^2 - R^2)\right] & R + P \leqslant x \leqslant R + Q,\ x > Q - R \\ \frac{1}{2} + \frac{3}{8x}\frac{P + Q}{P^2 + PQ + Q^2}\left[\frac{P^2 + Q^2}{2} + (x^2 - R^2)\right] & R - P \leqslant x \leqslant P + R,\ x \geqslant Q - R. \end{cases} \quad (56)$$

B.4. E(x, Q, R)

If point 1 is inside a sphere of radius Q, then the probability that its neighbor (point 2) at a distance x is outside the concentric sphere of radius R is $E(x, Q, R)$. We assume $a =$ the distance of point 1 from the center of the sphere.

(a) $R > Q$ and $x < R - Q$. All of the neighbors of point 1 are inside the sphere of radius R, giving $E(x, Q, R) = 0$.

(b) $R > Q$ and $R - Q < x < R$. Here $R - x < Q$. If $a < R - x$, all of the neighbors of point 1 are inside the sphere of radius R. For $a > R - x$, we can use Equation (54):

$$\begin{aligned} E(x, Q, R) &= \left[\frac{\frac{4\pi}{3}(R-x)^3}{\frac{4\pi}{3}Q^3}\right](0) \\ &\quad + \int_{R-x}^{Q}\left(1 - \frac{A(x,R,a)}{A_x}\right)\frac{4\pi a^2}{\frac{4\pi}{3}Q^3}da \\ &= \frac{1}{2} - \frac{R^3}{2Q^3} + \frac{3R^4}{16Q^3x} - \frac{3R^2}{8Qx} + \frac{3Q}{16x} \\ &\quad + \frac{3R^2x}{8Q^3} + \frac{3x}{8Q} - \frac{x^3}{16Q^3}. \end{aligned}$$

(c) $R > Q$ and $R < x < R + Q$. Here $x - R < Q$. If $a < x - R$, all of the neighbors of point 1 are outside the sphere of radius R:

$$\begin{aligned} E(x, Q, R) &= \left[\frac{\frac{4\pi}{3}(x-R)^3}{\frac{4\pi}{3}Q^3}\right](1) \\ &\quad + \int_{x-R}^{Q}\left(1 - \frac{A(x,R,a)}{A_x}\right)\frac{4\pi a^2}{\frac{4\pi}{3}Q^3}da \\ &= \frac{1}{2} - \frac{R^3}{2Q^3} + \frac{3R^4}{16Q^3x} - \frac{3R^2}{8Qx} + \frac{3Q}{16x} \\ &\quad + \frac{3R^2x}{8Q^3} + \frac{3x}{8Q} - \frac{x^3}{16Q^3}. \end{aligned}$$

(d) $R + Q < x$. All of the neighbors of point 1 are outside the sphere of radius R, giving $E(x, Q, R) = 1$.

(e) $Q > R$, $x < Q - R$, and $x < R$. Here $R - x > 0$ and $x + R < Q$. If $a < R - x$, all of the neighbors of point 1 are inside the sphere of radius R. If $a > R + x$, all of the neighbors of point 1 are inside the sphere of radius R:

$$\begin{aligned} E(x, Q, R) &= \left[\frac{\frac{4\pi}{3}(R-x)^3}{\frac{4\pi}{3}Q^3}\right](0) \\ &\quad + \int_{R-x}^{x+R}\left(1 - \frac{A(x,R,a)}{A_x}\right)\frac{4\pi a^2}{\frac{4\pi}{3}Q^3}da \\ &\quad + \left[\frac{\frac{4\pi}{3}(R+x)^3}{\frac{4\pi}{3}Q^3}\right](1) \\ &= 1 - \frac{R^3}{Q^3}. \end{aligned}$$

(f) $Q > R$, $x < Q - R$, and $R < x < Q + R$. Here $x - R > 0$ and $x + R < Q$. If $a < x - R$, all of the neighbors of point 1 are outside the sphere of radius R. If $a > R + x$, all of the neighbors of point 1 are inside the sphere of radius R:

$$\begin{aligned} E(x, Q, R) &= \left[\frac{\frac{4\pi}{3}(x-R)^3}{\frac{4\pi}{3}Q^3}\right](1) \\ &\quad + \int_{x-R}^{x+R}\left(1 - \frac{A(x,R,a)}{A_x}\right)\frac{4\pi a^2}{\frac{4\pi}{3}Q^3}da \\ &\quad + \left[\frac{\frac{4\pi}{3}(R+x)^3}{\frac{4\pi}{3}Q^3}\right](1) \\ &= 1 - \frac{R^3}{Q^3}. \end{aligned}$$

(g) $Q > R$, $x > Q - R$, and $x < R$. Here $R - x > 0$. If $a < R - x$, all of the neighbors of point 1 are inside the sphere of radius R:

$$\begin{aligned} E(x, Q, R) &= \left[\frac{\frac{4\pi}{3}(R-x)^3}{\frac{4\pi}{3}Q^3}\right](0) \\ &\quad + \int_{R-x}^{Q}\left(1 - \frac{A(x,R,a)}{A_x}\right)\frac{4\pi a^2}{\frac{4\pi}{3}Q^3}da \\ &= \frac{1}{2} - \frac{R^3}{2Q^3} + \frac{3R^4}{16Q^3x} - \frac{3R^2}{8Qx} \\ &\quad + \frac{3Q}{16x} + \frac{3R^2x}{8Q^3} + \frac{3x}{8Q} - \frac{x^3}{16Q^3}. \end{aligned}$$

(h) $Q > R$, $x > Q - R$, and $R < x < Q + R$. Here $x - R > 0$. If $a < x - R$, all of the neighbors of point 1 are outside the sphere of radius R:

$$\begin{aligned} E(x, Q, R) &= \left[\frac{\frac{4\pi}{3}(x-R)^3}{\frac{4\pi}{3}Q^3}\right](1) \\ &\quad + \int_{x-R}^{Q}\left(1 - \frac{A(x,R,a)}{A_x}\right)\frac{4\pi a^2}{\frac{4\pi}{3}Q^3}da \\ &= \frac{1}{2} - \frac{R^3}{2Q^3} + \frac{3R^4}{16Q^3x} - \frac{3R^2}{8Qx} \\ &\quad + \frac{3Q}{16x} + \frac{3R^2x}{8Q^3} + \frac{3x}{8Q} - \frac{x^3}{16Q^3} \end{aligned}$$

$$E(x, Q, R) = \begin{cases} 0 & x < R - Q \\ 1 - \frac{R^3}{Q^3} & R - Q < x < Q - R \\ \frac{1}{2} - \frac{R^3}{2Q^3} + \frac{3R^4}{16Q^3x} - \frac{3R^2}{8Qx} + \frac{3Q}{16x} + \frac{3R^2x}{8Q^3} + \frac{3x}{8Q} - \frac{x^3}{16Q^3} & |R - Q| < x < R + Q \\ 1 & x > R + Q. \end{cases} \quad (57)$$

This can also be derived using $E(x, Q, R) = C(x, 0, Q, R)$.

B.5. D(x, R)

If point 1 is inside a sphere of radius R, then the probability that its neighbor (point 2) at a distance x is outside the sphere is $D(x, R)$. We assume $a =$ the distance of point 1 from the center of the sphere.

(a) $x < R$. If $a < R - x$, then all of the neighbors of point 1 are inside the sphere. For $a > R - x$, we can use Equation (54):

$$D(x, R) = \left[\frac{\frac{4\pi}{3}(R-x)^3}{\frac{4\pi}{3}R^3}\right](0) + \int_{R-x}^{R}\left(1 - \frac{A(x, R, a)}{A_x}\right)\frac{4\pi a^2}{\frac{4\pi}{3}R^3}da = \frac{3x}{4R} - \frac{x^3}{16R^3}.$$

(b) $R < x < 2R$. If $a < x - R$, then all of the neighbors of point 1 are outside the sphere. For $a > x - R$, we can use Equation (54):

$$D(x, R) = \left[\frac{\frac{4\pi}{3}(x-R)^3}{\frac{4\pi}{3}R^3}\right](1) + \int_{x-R}^{R}\left(1 - \frac{A(x, R, a)}{A_x}\right)\frac{4\pi a^2}{\frac{4\pi}{3}R_x^3}da = \frac{3x}{4R} - \frac{x^3}{16R^3}.$$

(c) $2R < x$. All of the neighbors of point 1 are outside the sphere, giving $D(x, R) = 1$:

$$D(x, R) = \begin{cases} \frac{3x}{4R} - \frac{x^3}{16R^3} & x < 2R \\ 1 & x > 2R. \end{cases} \quad (58)$$

This can also be derived using $D(x, R) = E(x, R, R) = C(x, 0, R, R)$.

B.6. Fourier Transform of $1 - C(x, P, Q, R)$

As $C(x, P, Q, R)$ goes to unity at large x, we rearrange the terms of the correlation function so that we only have to deal with $1 - C(x, P, Q, R)$, which vanishes in this limit.

To take the Fourier transform of $1 - C(x, P, Q, R)$, we can take six subcases: (1) $R \leqslant P < Q$ and $P + R \leqslant Q - R$; (2) $R \leqslant P < Q$ and $Q - R \leqslant P + R$; (3) $P \leqslant R \leqslant Q$ and $Q - R \leqslant R - P$; (4) $P \leqslant R \leqslant Q$ and $R - P \leqslant Q - R \leqslant R + P$; (5) $P \leqslant R \leqslant Q$ and $R + P \leqslant Q - R$; and (6) $P < Q \leqslant R$. We can take the cases of $C(x, P, Q, R)$ for different limits for different cases. However, simplifying them, we get the following common form:

$$\begin{aligned}\text{F.T.}(1 - C(x, P, Q, R)) = {} & \frac{3}{64k^4\pi^4(P^3 - Q^3)} \\ & (-(1 + 2k^2\pi^2(Q + R)^2)\text{Cos}(2k\pi(Q - R)) \\ & - (1 + 2k^2\pi^2(P - R)^2)\text{Cos}(2k\pi(P + R)) \\ & + (1 + 2k^2\pi^2(Q - R)^2)\text{Cos}(2k\pi(Q + R)) \\ & + (1 + 2k^2\pi^2(P + R)^2)\text{Cos}(2k\pi(P - R)) \\ & + 2k\pi(+(-1 + 2k^2\pi^2(P - R)^2)(R + P)\text{Sin}(2k\pi(P + R)) \\ & - (-1 + 2k^2\pi^2(Q - R)^2)(Q + R)\text{Sin}(2k\pi(Q + R)) \\ & - (-1 + 2k^2\pi^2(P + R)^2)(P - R)\text{Sin}(2k\pi(P - R)) \\ & + (-1 + 2k^2\pi^2(Q + R)^2)(Q - R)\text{Sin}(2k\pi(Q - R))) \\ & + 8k^4\pi^4(-(P^2 - R^2)^2(\text{Ci}(P + R) - \text{Ci}(|P - R|)) \\ & + (Q^2 - R^2)^2(\text{Ci}(Q + R) - \text{Ci}(|Q - R|)))).\end{aligned}$$

The different cases mentioned above give different limits for the cos integral (Ci) function. They can be rearranged to make sure that the argument of the Ci function is always positive. To ensure the power spectrum is a positive definite function, we extract the symmetric part of the resulting expressions.

Appendix C
Correlation of Bubble Centers

C.1. Correlation of Ionized and Heated Regions

If there are ionization bubbles of only radius R_x, and if we assume there is no correlation between the ionization bubble centers, then the probability of a point at a distance r from the center of an ionized bubble to be ionized is

$$P_0 = f_i = \frac{4\pi}{3}R_x^3 N(R_x),$$

where $N(R_x) =$ the number density of the bubbles. Now, if we assume that there is a correlation between the ionization bubble centers, then this probability changes. The probability of a point located at a distance r in a shell of width Δr to be ionized is

$$P = \int_{r-\Delta r/2-R_x}^{r+\Delta r/2+R_x} \frac{4\pi x^2(1 + F(x))N(R_x)dx}{\frac{4\pi}{3}\left[\left(r + \frac{\Delta r}{2}\right)^3 - \left(r - \frac{\Delta r}{2}\right)^3\right]} \times \left[V\left(R_x, r + \frac{\Delta r}{2}, x\right) - V\left(R_x, r - \frac{\Delta r}{2}, x\right)\right],$$

where $F(x)$ is the correlation function of the ionization bubble centers at a distance x. This gives

$$P = \frac{4\pi}{3}N(R_x)R_x^3 + \int_{r-\Delta r/2-R_x}^{r+\Delta r/2+R_x} \frac{4\pi x^2 F(x)N(R_x)dx}{\frac{4\pi}{3}\left[\left(r + \frac{\Delta r}{2}\right)^3 - \left(r - \frac{\Delta r}{2}\right)^3\right]} \times \left[V\left(R_x, r + \frac{\Delta r}{2}, x\right) - V\left(R_x, r - \frac{\Delta r}{2}, x\right)\right].$$

For $\Delta r \to 0$, we have

$$P = f_i \Bigg(1 + \int_{r-\Delta r/2-R_x}^{r+\Delta r/2+R_x} \frac{9x^2 F(x)dx}{4\pi R_x^3 \left[\left(r+\frac{\Delta r}{2}\right)^3 - \left(r-\frac{\Delta r}{2}\right)^3 \right]} \times \left[V\left(R_x, r+\frac{\Delta r}{2}, x\right) - V\left(R_x, r-\frac{\Delta r}{2}, x\right) \right] \Bigg) = f_i(1 + G_i(r, R_x)). \tag{59}$$

Hence, we can get the probability of there being an ionized region at a distance r from the center of an ionized bubble if we have a nonzero correlation between the ionization bubble centers. Using the same method as above, we can also get the probability of there being a heated region at a distance r from the center of an ionized bubble given the correlation between the bubble centers:

$$P_h = f_i(1 + G_h(r, R_x, R_h)). \tag{60}$$

C.2. A Simple Model: One Bubble Size, Flat Heating Profile

To analyze the effect of the correlation between the ionization bubble centers, we can again study the simple model introduced in Section 3.5. Due to the correlation of the bubble centers, the overlap of bubbles increases, which decreases the heated volume fraction. It also modifies the expression for total correlation:

$$\begin{aligned}\mu = {} & (\psi_h^2 f_h + \psi_b^2 f_b) - (f_h \psi_h + f_b \psi_b)^2 \\ & + \int_{R_h}^{R_h+r} ((\psi_h - \psi_b)^2 f_h (1 - f_i(1 + G_i(y)) \\ & - f_h(1 + G_h(y))) \frac{dC(r, R_x, R_h, y)}{dy} \\ & + (\psi_b^2 f_i (1 - f_i(1 + G_i(y)) - f_h(1 + G_h(y))) \\ & + \psi_h^2 f_i f_h (1 + G_h(y))) \frac{dC(r, 0, R_x, y)}{dy} \Bigg) dy \\ & + \int_{R_x}^{R_h} \psi_h^2 f_i (1 - f_i(1 + G_i(y))) \frac{dC(r, 0, R_x, y)}{dy} dy.\end{aligned} \tag{61}$$

Here we assume that the correlation of the ionization bubble centers follows the same form as the density autocorrelation $F(r) = b\xi(r)$ with a constant bias b. We take two possible values of bias: $b = 1$ (no bias) and $b = 2$. Figure 17 shows the modified correlation for these two cases for the model considered in Figure 10. We notice that the H I signal increases due to the correlation of the ionization bubble centers. This effect is more significant at later times and on larger scales. The effect of the ionization bubble centers might also introduce correlations on scales at which the signal would be very small or zero without the bubble center correlations, e.g., the correlation at $r = 5$ Mpc in Figure 17.

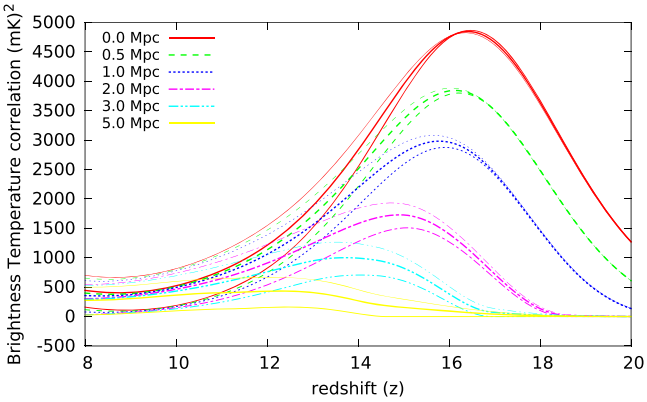

Figure 17. Evolution of the correlation function for a set of scales for a model in which the background temperature is held constant. The curves from bottom to top show the cases for no correlation, correlation with $b = 1$, and correlation with $b = 2$.

ORCID iDs

Janakee Raste https://orcid.org/0000-0001-7451-6139

References

Ahn, K., Mesinger, A., Alvarez, M. A., & Chen, X. 2015a, in Advancing Astrophysics with the Square Kilometre Array (AASKA14), Epoch of Reionisation (Trieste: SISSA), 3
Ahn, K., Xu, H., Norman, M. L., Alvarez, M. A., & Wise, J. H. 2015b, ApJ, 802, 8
Ali, Z. S., Parsons, A. R., Zheng, H., et al. 2015, ApJ, 809, 61
Barkana, R., & Loeb, A. 2001, PhR, 349, 125
Beardsley, A. P., Hazelton, B. J., Sullivan, I. S., et al. 2016, ApJ, 833, 102
Becker, R. H., Fan, X., White, R. L., et al. 2001, AJ, 122, 2850
Chen, X., & Miralda-Escudé, J. 2004, ApJ, 602, 1
Chen, X., & Miralda-Escudé, J. 2008, ApJ, 684, 18
Dodelson, S. 2003, Modern Cosmology (New York: Academic)
Fan, X., White, R. L., Davis, M., et al. 2000, AJ, 120, 1167
Fialkov, A., Barkana, R., & Cohen, A. 2015, PhRvL, 114, 101303
Fialkov, A., Barkana, R., & Visbal, E. 2014, Natur, 506, 197
Fialkov, A., Cohen, A., Barkana, R., & Silk, J. 2017, MNRAS, 464, 3498
Field, G. B. 1958, PIRE, 46, 240
Field, G. B. 1959, ApJ, 129, 551
Furlanetto, S. R., Zaldarriaga, M., & Hernquist, L. 2004a, ApJ, 613, 1
Furlanetto, S. R., Zaldarriaga, M., & Hernquist, L. 2004b, ApJ, 613, 16
Ghara, R., Choudhury, T. R., & Datta, K. K. 2015, MNRAS, 447, 1806
Gnedin, N. Y., & Shaver, P. A. 2004, ApJ, 608, 611
Hinshaw, G., Larson, D., Komatsu, E., et al. 2013, ApJS, 208, 19
Koopmans, L., Pritchard, J., Mellema, G., et al. 2015, in Advancing Astrophysics with the Square Kilometre Array (AASKA14), Epoch of Reionisation (Trieste: SISSA), 1
Madau, P., Meiksin, A., & Rees, M. J. 1997, ApJ, 475, 429
Mesinger, A., Ewall-Wice, A., & Hewitt, J. 2014, MNRAS, 439, 3262
Mesinger, A., Ferrara, A., & Spiegel, D. S. 2013, MNRAS, 431, 621
Mesinger, A., Furlanetto, S., & Cen, R. 2011, MNRAS, 411, 955
Morales, M. F., & Wyithe, J. S. B. 2010, ARA&A, 48, 127
Natarajan, A., & Yoshida, N. 2014, PTEP, 2014, 06B112
Osterbrock, D. E. 1989, Astrophysics of Gaseous Nebulae and Active Galactic Nuclei (Mill Valley, CA: Univ. Science Books)
Paciga, G., Albert, J. G., Bandura, K., et al. 2013, MNRAS, 433, 639
Pacucci, F., Mesinger, A., Mineo, S., & Ferrara, A. 2014, MNRAS, 443, 678
Patil, A. H., Yatawatta, S., Koopmans, L. V. E., et al. 2017, ApJ, 838, 65

Planck Collaboration, Adam, R., Aghanim, N., et al. 2016, A&A, 596, A108
Planck Collaboration, Ade, P. A. R., Aghanim, N., et al. 2014, A&A, 571, A16
Planck Collaboration, Ade, P. A. R., Aghanim, N., et al. 2016, A&A, 594, A13
Pritchard, J. R., & Furlanetto, S. R. 2007, MNRAS, 376, 1680
Pritchard, J. R., & Loeb, A. 2012, RPPh, 75, 086901
Rybicki, G. B., & dell'Antonio, I. P. 1994, ApJ, 427, 603
Sarkar, A., Mondal, R., Das, S., et al. 2016, JCAP, 4, 012
Sethi, S., & Haiman, Z. 2008, ApJ, 673, 1
Sethi, S. K. 2005, MNRAS, 363, 818
Sethi, S. K., & Subramanian, K. 2009, JCAP, 11, 021
Shaver, P. A., Windhorst, R. A., Madau, P., & de Bruyn, A. G. 1999, A&A, 345, 380
Sheth, R. K. 1998, MNRAS, 300, 1057
Shull, J. M., & van Steenberg, M. E. 1985, ApJ, 298, 268
Tashiro, H., & Sugiyama, N. 2013, MNRAS, 435, 3001
Tozzi, P., Madau, P., Meiksin, A., & Rees, M. J. 2000, NuPhS, 80, 05
Venkatesan, A., & Benson, A. 2011, MNRAS, 417, 2264
Venkatesan, A., Giroux, M. L., & Shull, J. M. 2001, ApJ, 563, 1
Visbal, E., Barkana, R., Fialkov, A., Tseliakhovich, D., & Hirata, C. M. 2012, Natur, 487, 70
Zaldarriaga, M., Furlanetto, S. R., & Hernquist, L. 2004, ApJ, 608, 622